Journal of the Mechanical Behavior of Biomedical Materials 179 (2026) 107423

Contents lists available at ScienceDirect

Journal of the Mechanical Behavior of Biomedical Materials

journal homepage: www.elsevier.com/locate/jmbbm

Research paper

A systematic comparison of membrane, shell, and 3D solid formulations for nonlinear vascular biomechanics

Taeouk Kim[a,*,1], Rogelio Ortigosa[b,1], Nitesh Nama[c,d,1], Miquel Aguirre[e,f,g], Antonio J. Gil[h], Jay D. Humphrey[i], C. Alberto Figueroa[a,j]

[a] Department of Biomedical Engineering, University of Michigan, Ann Arbor, MI, USA
[b] Computational Mechanics and Scientific Computing Group, Technical University of Cartagena, Campus Muralla del Mar, 30202, Cartagena Murcia, Spain
[c] Department of Mechanical & Materials Engineering, University of Nebraska-Lincoln, Lincoln, NE, USA
[d] Nebraska Center for Integrated Biomolecular Communication, University of Nebraska-Lincoln, Lincoln, NE, USA
[e] Laboratori de Càlcul Numèric, Universitat Politècnica de Catalunya, Jordi Girona 1, E-08034, Barcelona, Spain
[f] International Centre for Numerical Methods in Engineering (CIMNE), Gran Capità, 08034, Barcelona, Spain
[g] Mines Saint-Étienne, Univ Lyon, Univ Jean Monnet, INSERM, U 1059 Sainbiose, Centre CIS, F - 42023 Saint-Étienne, France
[h] Zienkiewicz Institute for Modelling, Data and AI, Faculty of Science and Engineering, Swansea University, Bay Campus, SA1 8EN, UK
[i] Department of Biomedical Engineering, Yale University, New Haven, CT, USA
[j] Department of Surgery, University of Michigan, Ann Arbor, MI, USA

ARTICLE INFO

Keywords:
Nonlinear membrane
Rotation free shell
Arterial wall mechanics

ABSTRACT

Typical computational methods for vascular biosolid mechanics represent the blood vessel wall as a membrane, shell, or 3D solid. Each of these formulations has advantages and disadvantages concerning accuracy, ease of implementation, and computational costs. Despite the widespread use of these formulations, a systematic comparison of the performance and accuracy of these formulations for nonlinear vascular biomechanics has remained wanting. Therefore, the decision regarding the optimal choice often relies on intuition or previous experience, with unclear consequences of choosing one approach over the other. Here, we present a systematic comparison among three different formulations to represent the vessel wall as: (i) a nonlinear membrane, (ii) a nonlinear, rotation-free shell, and (iii) a nonlinear 3D solid. For the 3D solid model, we consider two different implementations employing linear and quadratic interpolation. Convergence analysis for displacement and stress are presented for all formulations. We compare results in both idealized and subject-specific mouse aortic geometries. For the idealized cylindrical geometry, we compare our results against the axisymmetric solution for five different wall thickness-to-radius ratios. Subsequently, a comparison of these approaches is presented for an idealized arterial bifurcation having regionally varying wall thickness. Lastly, we compare results for a subject-specific mouse geometry with regionally varying material properties and wall thickness. External tissue support boundary conditions model the effect of perivascular tissue. Based on our results, the rotation-free shell formulation represents the most advantageous compromise between computational cost and accuracy for large scale vascular biomechanics applications that include complex geometries.

1. Introduction

Computational methods to simulate cardiovascular biomechanics in three-dimensional (3D) models of arteries have attracted significant interest owing to their applications in disease research, medical device design, and surgical planning (Lally et al., 2005; Figueroa et al., 2009; Laubrie et al., 2020; Raghavan et al., 2000; Humphrey, 2013; Maas et al., 2012; Kim et al., 2023a,b). Computational models have utilized various representations of the vascular wall which has been modeled, with varying degrees of detail, as either a 3D solid or a two-dimensional (2D) structure (membrane or shell). The latter choice has been motivated by the low ratio of wall thickness to radius exhibited by most arteries and veins as well as the presence of residual stresses, which tend to homogenize transmural distributions of wall stress and thereby render 2D solutions as good approximations in many cases (Humphrey and Rajagopal, 2002). Nonetheless, each of these approaches has its advantages and disadvantages concerning computational efficiency, accuracy, and ease of implementation.

---

[*] Corresponding author.
E-mail addresses: taeouk@umich.edu (T. Kim), figueroc@med.umich.edu (C.A. Figueroa).
[1] Authors contributed equally to this work.

https://doi.org/10.1016/j.jmbbm.2026.107423
Received 19 September 2025; Received in revised form 13 March 2026; Accepted 29 March 2026

In general, 3D solid models offer excellent accuracy, straightforward implementation, and flexibility to incorporate arbitrary constitutive material models and distributions of properties across the layered wall (Wriggers et al., 1996). They have been extensively employed both for the solid mechanics analysis of arterial wall (Doyle et al., 2007; Weisbecker et al., 2014; Liu et al., 2017; Lally et al., 2005; Riveros et al., 2013) and fluid–structure analyses (Gerbeau et al., 2005; Colciago et al., 2014; Bazilevs et al., 2010). Nevertheless, 3D solid models employing low-order interpolation can present significant challenges concerning various locking phenomena and difficulty in generating good quality meshes for thin geometries. Specifically, generating a sufficiently good mesh (i.e., with an appropriate aspect ratio of mesh elements) for thin geometries requires a finer in-plane mesh, leading to significant increases in degrees of freedom. This challenge can, in principle, be circumvented via the use of higher-order interpolation in 3D solid formulations. However, such formulations are typically undesirable for vascular applications owing to their associated numerical instabilities and high computational cost.

To circumvent these challenges, 2D manifold representations of the vessel wall have been proposed. Earlier works have employed a membrane representation of the vessel wall and highlighted its significantly lower computational cost. For example, the vessel wall has been modeled as either a linear (Figueroa et al., 2006) or a nonlinear (Lu et al., 2008; Kyriacou et al., 1996; Gil, 2006; Gil and Bonet, 2006, 2007) membrane. More recently, various shell models have been employed to incorporate the bending stiffness of the vessel wall (Kim et al., 2008; Tepole et al., 2015; Zhou et al., 2010; Laubrie et al., 2020; Martin et al., 2015; Nama et al., 2020). While shell theory is a mature field in nonlinear mechanics (Bischoff et al., 2004; Remmers et al., 2003; Hosseini et al., 2013, 2014; Hughes and Carnoy, 1983), adaptation of these theories for vascular biomechanics is largely restricted to shell formulations that employ the Kirchhoff–Love theory. In particular, consider the recent stress resultant shell formulation employed by Kim et al. (2008)(in the context of heart valve leaflets), the isogeometric formulation by Tepole et al. (2015), and our recent work using a rotation-free shell formulation (Nama et al., 2020). We also note that subject-specific geometric models are typically obtained from medical images, where a direct assessment of vessel wall thickness is difficult. Consequently, construction of a 3D volumetric geometric model of the vessel wall entails creation of a surface mesh that is then extended radially to obtain a 3D solid mesh. In this context, 2D representations offer another advantage over 3D models by avoiding the need for this additional pre-processing step.

Nevertheless, despite the widespread use of 2D models of vascular walls, there is limited understanding of the relative advantages and disadvantages of their performance against 3D solid formulations (Wriggers et al., 1996; Chen, 2004). To the best of our knowledge, there has been no comprehensive comparison of these approaches in the context of vascular biomechanics for complex subject-specific geometries and biologically relevant material models. Consequently, the modeling choice often relies on intuition and preference, with unclear consequences of choosing one approach over the other.

Another issue that introduces differences between 2D and 3D models concerns the handling of incompressibility. Typically, 3D models do not enforce incompressibility exactly to avoid the introduction of a Lagrange multiplier. Instead, they enforce near incompressibility. By contrast, 2D representations of vessel wall enforce incompressibility exactly by expressing through-the-thickness quantities in terms of in-plane quantities. The consequences of this difference in handling incompressibility are unclear.

Here, we address this gap in the literature by presenting a systematic comparison of three different approaches of modeling the nonlinear mechanics of the vascular wall. The first is a nonlinear membrane model used previously by Lu et al. (2008) for cerebral aneurysms. The second is a nonlinear, rotation-free shell model, originally proposed by Oñate and Flores (2005), and recently adapted for biomechanics by Nama et al. (2020). The third is a nonlinear 3D solid model, where we consider two different implementations employing wedge (or triangular prismatic) elements with linear and quadratic interpolation, which will be referred to as P1 and P2 models respectively (Zienkiewicz et al., 2005; Yamakawa and Shimada, 2009; Afazov et al., 2012; Meftah et al., 2021).

The outline of rest of the article is as follows: In Section 2, we briefly describe each formulation with an emphasis on assumptions concerning through-the-thickness variations of kinematic quantities. We also highlight differences in handling the incompressibility condition among these approaches. We then describe our strategy to obtain 3D solid wedge elements from the 2D midsurface triangular elements to ensure a consistent comparison among different formulations. In Section 3, we contrast results across the different formulations. We first consider an idealized cylindrical geometry to compare results of each formulation against the axisymmetric theory and investigate the performance of different formulations as a function of wall thickness to radius ratio. We also compare the performance of different formulations in an idealized arterial bifurcation with regionally varying wall thickness. We then compare results for a subject-specific mouse geometry with regionally varying material properties and wall thickness. Lastly, we discuss of our results in Section 4.

2. Theoretical formulation

For each of the three basic formulations, we consider the mapping of a point within a neighborhood of the body from its initial configuration to any deformed configuration (Fig. 1). Subsequently, we utilize this mapping to construct the deformation gradient tensor and right Cauchy–Green tensor. These expressions are then employed to define the elastic strain energy for the two constitutive models considered.

Below, Greek subscripts or superscripts take values $\{1, 2\}$ while Latin subscripts or superscripts take values $\{1, 2, 3\}$. We follow Einstein's index notation where a repeated symbol denotes a summation, unless stated otherwise; $\boldsymbol{x}$ and $\boldsymbol{X}$ locate a point in the continuum in current and initial configurations, respectively, while $\boldsymbol{\varphi}$ and $\boldsymbol{\varphi}^{(0)}$ locate a point on the midsurface of the continuum in current and initial configurations, respectively.

2.1. Kinematics

2.1.1. Membrane formulation

Consider the nonlinear membrane formulation, previously employed by Lu et al. (2007) for cerebral aneurysms. Membrane formulations represent the simplest modeling choice for the vessel wall and describe the kinematics via mid-surface quantities (Gruttmann and Taylor, 1992).

Consider a mapping between $\boldsymbol{\varphi}^{(0)}$ and $\boldsymbol{\varphi}$, both belonging to the membrane surface. The surface is parameterized by convective coordinates ξ^{α} $(\alpha = 1, 2)$, which yield a basis of two covariant vectors in the tangent planes of the initial and deformed configurations

$$\mathbf{B}_{\alpha} = \frac{\partial \boldsymbol{\varphi}^{(0)}}{\partial \xi^{\alpha}}, \quad \mathbf{b}_{\alpha} = \frac{\partial \boldsymbol{\varphi}}{\partial \xi^{\alpha}}. \tag{1}$$

The corresponding contravariant vectors can be obtained as follows

$$\mathbf{B}^{\alpha} = B^{\alpha\beta}\mathbf{B}_{\beta}, \quad \mathbf{b}^{\alpha} = b^{\alpha\beta}\mathbf{b}_{\beta}, \tag{2}$$

where $B^{\alpha\beta} = \mathbf{B}^{\alpha} \cdot \mathbf{B}^{\beta}$ and $b^{\alpha\beta} = \mathbf{b}^{\alpha} \cdot \mathbf{b}^{\beta}$. Following Gruttman and Taylor (Gruttmann and Taylor, 1992), we introduce an orthonormal basis in the material configuration; in this case the covariant and contravariant components of the referential stress and strain tensors are identical, thereby simplifying the implementation. To this end, we define

$$\mathbf{A}_3 = \mathbf{A}^3 = \frac{\mathbf{B}_1 \times \mathbf{B}_2}{\|\mathbf{B}_1 \times \mathbf{B}_2\|}, \quad \mathbf{A}_1 = \mathbf{A}^1 = \frac{\mathbf{B}_1}{\|\mathbf{B}_1\|}, \quad \mathbf{A}_2 = \mathbf{A}^2 = \mathbf{A}_3 \times \mathbf{A}_1, \tag{3}$$

with associated coordinates s_α indirectly defined as

$$\mathbf{A}_\alpha = \mathbf{A}^\alpha = \frac{\partial \boldsymbol{\varphi}^{(0)}}{\partial s_\alpha}. \tag{4}$$

We remark that this orthonormal basis is introduced for mathematical convenience and ease of implementation and is not strictly necessary to describe the membrane formulation. Similarly, the basis vectors (not necessarily orthonormal) at a position $\boldsymbol{\varphi}$ of a point on the membrane surface in the current configuration can be defined as

$$\mathbf{a}_\alpha = \frac{\partial \boldsymbol{\varphi}}{\partial s_\alpha}. \tag{5}$$

Fig. 1(A) shows the initial and deformed configurations of the vessel wall midsurface and the corresponding basis. The in-plane deformation gradient can be defined as

$$\bar{\mathbf{F}} = \frac{\partial \boldsymbol{\varphi}}{\partial \boldsymbol{\varphi}^{(0)}} = \frac{\partial \boldsymbol{\varphi}}{\partial s_\alpha} \otimes \frac{\partial s_\alpha}{\partial \boldsymbol{\varphi}^{(0)}} = \mathbf{a}_\alpha \otimes \mathbf{A}^\alpha. \tag{6}$$

Correspondingly, the in-plane right Cauchy–Green tensor is obtained as

$$\bar{\mathbf{C}} = a_{\alpha\beta}\mathbf{A}^\alpha \otimes \mathbf{A}^\beta, \tag{7}$$

where $a_{\alpha\beta}$ denotes the metric in the current configuration

$$a_{\alpha\beta} = \mathbf{a}_\alpha \cdot \mathbf{a}_\beta. \tag{8}$$

We remark that the membrane strain can be described completely without requiring an explicit reference to the underlying 3D deformation. Nonetheless, it is useful to view the midsurface deformation as components of the 3D motion. Neglecting the transverse shear strain, the corresponding 3D deformation gradient can be written as

$$\mathbf{F} = \mathbf{a}_\alpha \otimes \mathbf{A}^\alpha + \lambda_3 \mathbf{a}_3 \otimes \mathbf{A}_3, \tag{9}$$

where $\lambda_3 = h/H$ denotes the thickness stretch with h and H being the current and initial thickness of the membrane. Accordingly, the 3D right Cauchy–Green tensor is

$$\mathbf{C} = a_{\alpha\beta}\mathbf{A}^\alpha \otimes \mathbf{A}^\beta + \lambda_3^2 \mathbf{A}_3 \otimes \mathbf{A}_3. \tag{10}$$

with

$$C_{ij} = \begin{bmatrix} a_{11} & a_{12} & 0 \\ a_{21} & a_{22} & 0 \\ 0 & 0 & \lambda_3^2 \end{bmatrix}, \tag{11}$$

where C_{33} is obtained via plane stress and incompressibility conditions. This allows the Jacobian determinant to be expressed as

$$J = \sqrt{\det(\mathbf{C})} = J_0 \lambda_3, \tag{12}$$

where $J_0 = \sqrt{\frac{|a_{\alpha\beta}|}{|\mathbf{A}\alpha\beta|}}$ denotes the in-plane Jacobian determinant. Eq. (12), in combination with the incompressibility condition

$$J = 1, \tag{13}$$

yields

$$\lambda_3 = J_0^{-1}. \tag{14}$$

This coupling of out-of-plane components with the in-plane metrics ensures satisfaction of the incompressibility constraint. This approach enables us to employ general 3D constitutive models by relating 3D strain quantities to their in-plane counterparts, as described in Section 2.2.

2.1.2. Rotation-free shell formulation

Next, we describe the rotation-free shell formulation, originally proposed by Oñate and Flores (2005) and recently adapted for biomechanics by Nama et al. (2020). This shell formulation employs the Kirchhoff hypothesis of straight and normal cross-sections and describes the kinematics of vessel wall via its midsurface and associated normal vector. Below, we provide a brief overview of this formulation and refer the reader to our earlier work (Nama et al., 2020) for a more detailed description.

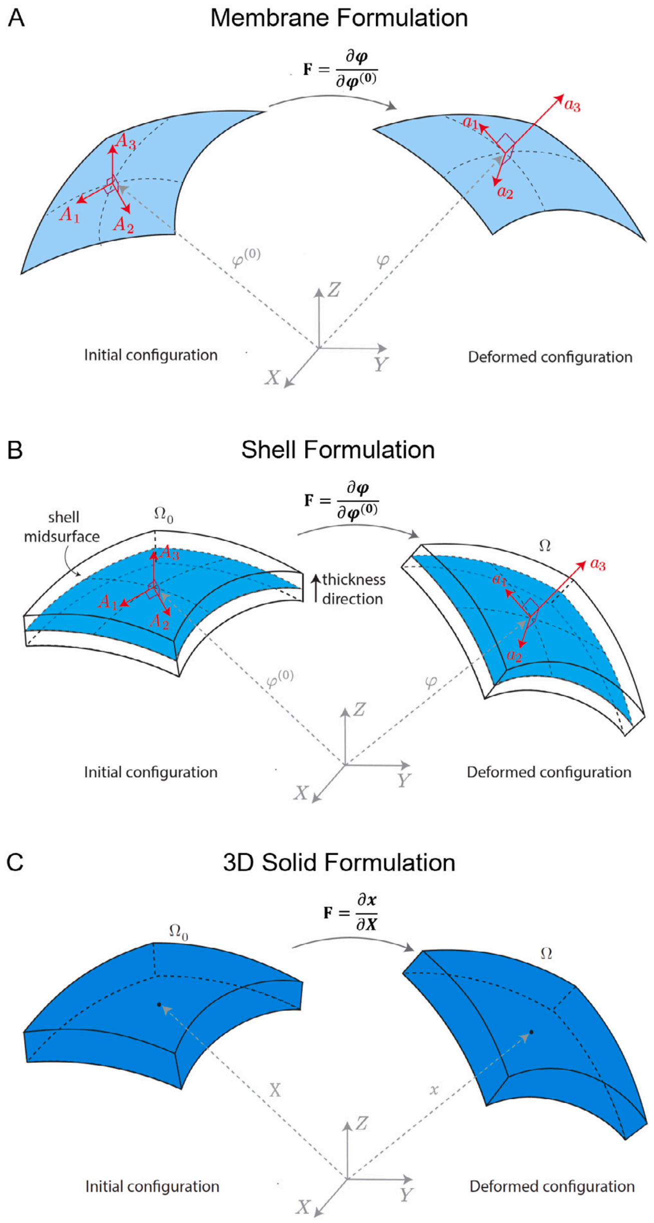

Fig. 1. Schematic drawing illustrating the basis vectors in the initial and deformed configurations for the three formulations. Note, the referential approach in which locations of points of interest in the body are referred back to a coordinate system for (X,Y,Z).

Consider Fig. 1(B) where $\boldsymbol{\varphi}^{(0)}$ again is mapped to $\boldsymbol{\varphi}$, with both belonging to the shell midsurface. Similar to the membrane formulation described above, and following Gruttmann and Taylor (1992), we define an orthonormal basis corresponding to a point with associated coordinates s_α on the shell midsurface in the initial configuration as

$$\mathbf{A}_\alpha = \frac{\partial \boldsymbol{\varphi}^{(0)}}{\partial s_\alpha}, \tag{15}$$

with the unit normal vector to the midsurface

$$\mathbf{A}_3 = \frac{\mathbf{A}_1 \times \mathbf{A}_2}{\|\mathbf{A}_1 \times \mathbf{A}_2\|}. \tag{16}$$

Again, as noted earlier in the discussion of membrane formulation, this orthonormal basis is introduced for mathematical convenience and ease of implementation and is not strictly necessary to describe the shell formulation. Similar to the initial configuration, the basis vectors (not necessarily orthonormal) at a position $\boldsymbol{\varphi}$ of a point on the shell midsurface in the current configuration can be defined as

$$\mathbf{a}_\alpha = \frac{\partial \boldsymbol{\varphi}}{\partial s_\alpha}, \qquad \mathbf{a}_3 = \frac{\mathbf{a}_1 \times \mathbf{a}_2}{\|\mathbf{a}_1 \times \mathbf{a}_2\|}. \tag{17}$$

These definitions allow us to express the positions, $\boldsymbol{X}$ and $\boldsymbol{x}$, of a general point in the initial and the deformed configuration, respectively, as

$$\boldsymbol{X} = \boldsymbol{\varphi}^{(0)} + \xi_3 \mathbf{A}_3, \tag{18}$$

$$\boldsymbol{x} = \boldsymbol{\varphi} + \xi_3 \lambda_3 \mathbf{a}_3, \tag{19}$$

where ξ_3 $(-\frac{H}{2} \leq \xi_3 \leq \frac{H}{2})$ denotes the perpendicular distance of the point to the midsurface with H the shell thickness in the reference configuration and $\lambda_3 = h/H$ denotes the thickness stretch with h the current thickness. We note that the thickness stretch represents an additional unknown quantity that is obtained via incompressibility and plane stress conditions, as described in Section 2.2.1.

The basis vectors, $\mathbf{G}_\alpha = \frac{\partial X}{\partial s_\alpha}$, at a general point in the shell continuum can be expressed in terms of midsurface basis vectors as

$$\mathbf{G}_\alpha = \mathbf{A}_\alpha + \xi_3 \mathbf{A}_{3,\alpha}, \tag{20}$$

$$\mathbf{G}_3 = \mathbf{A}_3, \tag{21}$$

where $(\cdot)_{,\alpha}$ denotes the partial derivative of a quantity with respect to s_α. The covariant metrics are

$$G_{\alpha\beta} = A_{\alpha\beta} + 2\xi_3 \kappa^{(0)}_{\alpha\beta} + \xi_3^2 \mathbf{A}_{3,\alpha} \cdot \mathbf{A}_{3,\beta}, \tag{22}$$

$$G_{\alpha 3} = G_{3\alpha} = \mathbf{A}_\alpha \cdot \mathbf{A}_3 + \xi_3 \mathbf{A}_{3,\alpha} \cdot \mathbf{A}_3 = 0, \tag{23}$$

$$G_{33} = A_{33} = 1, \tag{24}$$

where $A_{\alpha\beta}$ are components (first fundamental form) in the initial configuration given as

$$A_{\alpha\beta} = \mathbf{A}_\alpha \cdot \mathbf{A}_\beta, \tag{25}$$

and $\kappa^{(0)}_{\alpha\beta}$ are components of the curvature (second fundamental form) of the midsurface in the initial configuration given as

$$\kappa^{(0)}_{\alpha\beta} = \frac{1}{2}(\mathbf{A}_\alpha \cdot \mathbf{A}_{3,\beta} + \mathbf{A}_\beta \cdot \mathbf{A}_{3,\alpha}). \tag{26}$$

We linearize strain through the thickness and therefore neglect the quadratic term in Eq. (22) to obtain (Kiendl et al., 2015):

$$G_{\alpha\beta} = A_{\alpha\beta} + 2\xi_3 \kappa^{(0)}_{\alpha\beta}. \tag{27}$$

Similarly, using the basis vectors in the current configuration $\mathbf{g}_\alpha = \frac{\partial x}{\partial s_\alpha}$, the metrics in the current configuration are

$$g_{\alpha\beta} = a_{\alpha\beta} + 2\xi_3 \kappa_{\alpha\beta}, \tag{28}$$

with

$$a_{\alpha\beta} = \mathbf{a}_\alpha \cdot \mathbf{a}_\beta, \qquad \kappa_{\alpha\beta} = \frac{1}{2}(\mathbf{a}_\alpha \cdot \mathbf{a}_{3,\beta} + \mathbf{a}_\beta \cdot \mathbf{a}_{3,\alpha}). \tag{29}$$

Given our choice of orthonormal basis in the initial configuration, the metrics $A_{\alpha\beta}$ are equal to the components of the 2 × 2 identity tensor. Therefore, for surfaces with non-zero curvature in the initial configuration (i.e., $\kappa^{(0)}_{\alpha\beta} \neq 0$), the presence of the term $2\xi_3\kappa^{(0)}_{\alpha\beta}$ in Eq. (27) implies that the metrics $G_{\alpha\beta}$ are not equal to the components of the identity tensor, indicating a non-zero deformation even in the initial configuration. To mitigate this issue, we follow the approach by Flores and Onate (2005) to replace the curvature $\kappa_{\alpha\beta}$ by relative curvature $\chi_{\alpha\beta} = \kappa_{\alpha\beta} - \kappa^{(0)}_{\alpha\beta}$ in Eqs. (27) and (28). Accordingly, we approximate the covariant metrics in the current configuration as

$$g_{\alpha\beta} = a_{\alpha\beta} + 2\xi_3 \chi_{\alpha\beta}. \tag{30}$$

We remark that this approximation, while not strictly necessary, facilitates the use of standard constitutive material models (e.g., Eq. (39) given below) by enforcing that the metrics in initial configuration are components of a unit tensor.

Using the basis vectors defined in Eqs. (20) and (21) and their counterparts in the deformed configuration, $\mathbf{g}_i$, the deformation gradient is

$$\mathbf{F} = \frac{\partial \boldsymbol{x}}{\partial \boldsymbol{X}} = \frac{\partial \boldsymbol{x}}{\partial s_\alpha} \otimes \frac{\partial s_\alpha}{\partial \boldsymbol{X}} = \mathbf{g}_i \otimes \mathbf{G}^i, \tag{31}$$

and the right Cauchy–Green tensor is

$$\mathbf{C} = \mathbf{F}^{\mathrm{T}}\mathbf{F} = g_{ij}\mathbf{G}^i \otimes \mathbf{G}^j. \tag{32}$$

Here, the transverse components $g_{\alpha 3} = g_{3\alpha} = 0$ since $\mathbf{g}_\alpha \cdot \mathbf{g}_3 = 0$. Furthermore, Eq. (32) indicates that the covariant components of the right Cauchy–Green tensor and the metrics in the deformed configuration are identical. However, since $g_{33} = \mathbf{a}_3 \cdot \mathbf{a}_3 = 1$, this equation does not reflect the change in shell thickness. Consequently, to account for the radial (thickness) deformation, Eq. (32) needs to be replaced by (Kiendl et al., 2015)

$$\mathbf{C} = C_{ij}\mathbf{G}^i \otimes \mathbf{G}^j, \tag{33}$$

with

$$C_{ij} = \begin{bmatrix} g_{11} & g_{12} & 0 \\ g_{21} & g_{22} & 0 \\ 0 & 0 & C_{33} \end{bmatrix}, \tag{34}$$

where C_{33} is obtained via plane stress and incompressibility conditions. This allows the Jacobian determinant to be expressed as

$$J = \sqrt{\det(\mathbf{C})} = J_0\sqrt{C_{33}}, \tag{35}$$

where $J_0 = \sqrt{\frac{|g_{\alpha\beta}|}{|G_{\alpha\beta}|}}$ denotes the in-plane Jacobian determinant. Eq. (35), in combination with the incompressibility condition

$$J = 1, \tag{36}$$

yields

$$C_{33} = J_0^{-2}. \tag{37}$$

This coupling of out-of-plane components with the in-plane metrics ensures satisfaction of the incompressibility constraint.

2.1.3. Continuum formulation

Next, we describe a 3D nonlinear continuum formulation. Referring to Fig. 1(C), let $\Omega_0 \subset \mathbb{R}^3$, be an open, bounded and connected domain which represents the reference (or undeformed) configuration of the vessel wall. The deformation of the body Ω_0 is defined through the mapping $\boldsymbol{\phi} : \Omega_0 \to \mathbb{R}^3$ that links the position of a material point from the reference configuration $\boldsymbol{X} \in \Omega_0$ to one in the deformed configuration $\boldsymbol{x} \in \Omega$ according to $\boldsymbol{x} = \boldsymbol{\phi}(\boldsymbol{X})$ with $\Omega = \boldsymbol{\phi}(\Omega_0)$. Associated with the mapping $\boldsymbol{\phi}$, the deformation gradient tensor $\mathbf{F}$ and the right Cauchy–Green tensor $\mathbf{C}$ are defined as

$$\mathbf{F} = \frac{\partial \boldsymbol{x}}{\partial \boldsymbol{X}}, \qquad \mathbf{C} = \mathbf{F}^{\mathrm{T}}\mathbf{F}. \tag{38}$$

We remark that, in contrast to the membrane and shell formulations that enforce the incompressibility constraint exactly at the continuum level, the chosen continuum displacement-based formulation enforces quasi-incompressibility (see Section 2.2.1 for further details).

We further note that, as opposed to the shell and membrane formulations, the 3D formulation requires no assumptions concerning through-the-thickness variation of kinematic quantities other than those implicit in the choice of spatial interpolation. The strategy for the generation of the solid discretization as well as the different spatial interpolations considered for the 3D continuum formulation are discussed later in Section 2.3.

2.2. Constitutive models

Next, we describe the two different constitutive models considered. The expressions for the elastic strain energy provided below are standard representations of these constitutive models; however, these expressions are typically modified by introducing Lagrange multipliers or penalty terms (i.e. volumetric energy contributions) to enforce the incompressibility condition, as described in Section 2.2.1.

Mooney–Rivlin: The elastic strain energy for a Mooney–Rivlin model (commonly used to represent elastomers) is

$$\psi_{\text{el}} = c_1(I_C - 3) + c_2(II_C - 3), \tag{39}$$

where c_1, c_2 are material parameters and I_C, II_C are the first and second principal invariants of the right Cauchy–Green tensor $\mathbf{C}$ given as

$$I_C = \text{tr}(\mathbf{C}), \qquad II_C = \frac{1}{2}\left[\text{tr}(\mathbf{C})^2 - \text{tr}(\mathbf{C}^2)\right]. \tag{40}$$

For the special case of $c_2 = 0$, this model reduces to the neo-Hookean model.

Four-fiber family model: The four-fiber family model characterizes the arterial wall as a composite structure comprising an elastin-dominated isotropic matrix, four families of embedded collagen fibers, and passive smooth muscle (circumferentially oriented along with one collagen family). The elastic strain energy is (Eberth et al., 2011; Roccabianca et al., 2014; Ferruzzi et al., 2011)

$$\psi_{\text{el}} = \frac{c}{2}(I_C - 3) + \sum_{k=1}^{4} \frac{c_1^k}{4c_2^k}\left[e^{c_2^k[(\lambda^k)^2-1]^2} - 1\right], \tag{41}$$

where c, c_1^k, c_2^k are material parameters, I_C is again the first invariant of the right Cauchy–Green tensor and $\lambda^k = \sqrt{\mathbf{M}^k \cdot \mathbf{C}\mathbf{M}^k}$ is the stretch experienced by the kth fiber family that is oriented along the direction $\mathbf{M}^k = [0, \sin\alpha_0^k, \cos\alpha_0^k]$ in the reference configuration. The four-fiber families are considered to be aligned along $\alpha_0^1 = 0°$ (axial family), $\alpha_0^2 = 90°$ (circumferential family) and $\alpha_0^{3,4} = \pm\alpha_0$ (symmetric diagonal families), where α_0 is a free parameter. The four-fiber family model has recently been recommended as the first choice constitutive model to simulate arterial deformations that lie outside the range of experimental tests (Schroeder et al., 2018) and has been extensively employed to describe the behavior of both human and murine arterial tissue (Ferruzzi et al., 2011; Roccabianca et al., 2014).

2.2.1 Enforcement of incompressibility and plane stress

In this section, we briefly discuss the strategies to enforce the incompressibility constraint for each formulation considered in this work. Additionally, we discuss the plane stress condition employed in the membrane and shell formulations.

Membrane formulation: Here, we follow the strategy suggested by Lu et al. (2008) where the membrane deformation is viewed as components of a 3D motion. The corresponding 3D version of the in-plane right Cauchy–Green tensor, Eq. (7), is expressed as

$$\mathbf{C} = a_{\alpha\beta}\mathbf{A}^\alpha \otimes \mathbf{A}^\beta + \lambda_3^2 \mathbf{A}_3 \otimes \mathbf{A}_3, \tag{42}$$

where $\lambda_3 = h/H$ denotes the thickness stretch with h and H the current and initial thickness of the membrane, and $\mathbf{A}_3$ denotes the unit normal vector to the membrane surface. Using Eqs. (7) and (42), the 3D Jacobian determinant can be expressed as

$$J = \sqrt{\det(\mathbf{C})} = \bar{J}\lambda_3, \tag{43}$$

where $\bar{J} = \sqrt{\frac{\|\mathbf{a}_1 \times \mathbf{a}_2\|}{\|\mathbf{A}_1 \times \mathbf{A}_2\|}}$ denotes the in-plane Jacobian determinant. The incompressibility constraint is enforced by setting $J = 1$, which in combination with Eq. (43), yields

$$\lambda_3 = 1/\bar{J}. \tag{44}$$

This allows us to express the 3D strain invariants in terms of the in-plane invariants (7), as

$$I_C = \overline{I}_C + \overline{II}_C^{\,-1}, \qquad II_C = \overline{I}_C \overline{II}_C^{\,-1} + \overline{II}_C, \tag{45}$$

where

$$\overline{I}_C = \text{tr}(\bar{\mathbf{C}}), \qquad \overline{II}_C = \frac{1}{2}\left[\text{tr}(\bar{\mathbf{C}})^2 - \text{tr}(\bar{\mathbf{C}}^2)\right]. \tag{46}$$

where $\overline{C}$ is defined in Eq. (7) .

Therefore, the 3D right Cauchy–Green tensor (Eq. (42)) and consequently, the elastic strain energy (Eqs. (39) and (41)) can be completely described in terms of in-plane quantities. Furthermore, it can be shown that, under a plane stress condition, the in-plane components of the second Piola–Kirchhoff stress are given as $S^{\alpha\beta} = 2\frac{\partial\psi_{\text{el}}(\bar{\mathbf{C}})}{\partial a_{\alpha\beta}}$. We refer the reader to Lu et al. (2008) for further details on constitutive modeling in membrane formulation.

Rotation-free shell formulation: Here, we follow the strategy in Kiendl et al. (2009), Nama et al. (2020) where incompressibility is enforced by augmenting the elastic strain energy function $\psi_{\text{el}}(\mathbf{C})$ with a constraint term using a Lagrange multiplier p as

$$\psi = -p(J - 1) + \psi_{\text{el}}(\mathbf{C}). \tag{47}$$

Here, we again follow the same arguments as above to express the thickness stretch $\lambda_3 = h/H$ in terms of in-plane quantities, as in Eq. (44). Furthermore, the additional unknown p introduced in Eq. (47) can be determined using a plane stress condition (Kiendl et al., 2015). Following Kiendl et al. (2015), we first derive the 3D components of the second Piola–Kirchhoff stress tensor ($\mathbf{S} = S^{ij}\mathbf{G}_i \otimes \mathbf{G}_j$) while considering p to be a function of C_{ij} as

$$S^{ij} = 2\frac{\partial\psi}{\partial C_{ij}} = 2\frac{\partial\psi_{\text{el}}}{\partial C_{ij}} - 2\frac{\partial p}{\partial C_{ij}}(J - 1) - 2p\frac{\partial J}{\partial C_{ij}}. \tag{48}$$

Using the plane stress condition $S^{33} = 0$, with Eqs. (35), (36), (37), and (48), we obtain

$$p = 2\frac{\partial\psi_{\text{el}}}{\partial C_{33}}C_{33}. \tag{49}$$

A more detailed description of this strategy can be found in Kiendl et al. (2015) and our recent work Nama et al. (2020).

3D continuum formulation: It proves convenient computationally to modify Eq. (39) as

$$\psi_{\text{el}} = c_1(I_C - 3) + c_2(II_C - 3) - 2\left(c_1 + 2c_2\right)\ln J. \tag{50}$$

Similarly, for the four-fiber family model in Eq. (41), let

$$\psi_{\text{el}} = \frac{c}{2}(I_C - 3) + \sum_{k=1}^{4} \frac{c_1^k}{4c_2^k}\left[e^{c_2^k[(\lambda^k)^2-1]^2} - 1\right] - c\ln J, \tag{51}$$

where the last term in above Eqs. (50) and (51) represents appropriate contributions to ensure stress free conditions in the origin of deformations. There are various possibilities to enforce incompressibility here. One approach is to enforce full incompressibility, as in Eq. (47), by introducing a Lagrange multiplier p that weakly enforces $J = 1$. However, for the 3D continuum formulation, this entails the use of a mixed formulation with finite element spaces for both displacements and the Lagrange multiplier p which comply with the *inf-sup* or LBB condition (Boffi et al., 2013). Therefore, in this work, it proves convenient computationally to employ a displacement-based formulation where the incompressibility of the material is relaxed and enforced in a penalty-type manner by adding a volumetric term $U(J)$ (Bonet et al., 2016)

$$\psi = \psi_{\text{el}} + U(J); \qquad U(J) = \frac{\lambda}{2}(J - 1)^2, \tag{52}$$

with a sufficiently large value of the penalty parameter λ yielding a good approximation of the incompressibility of the material, with $\lambda \approx 10^2 \times 2\left(c_1 + c_2\right)$ for the model in Eq. (50) and $\lambda = 10^2 \times c$ for the model in Eq. (51).

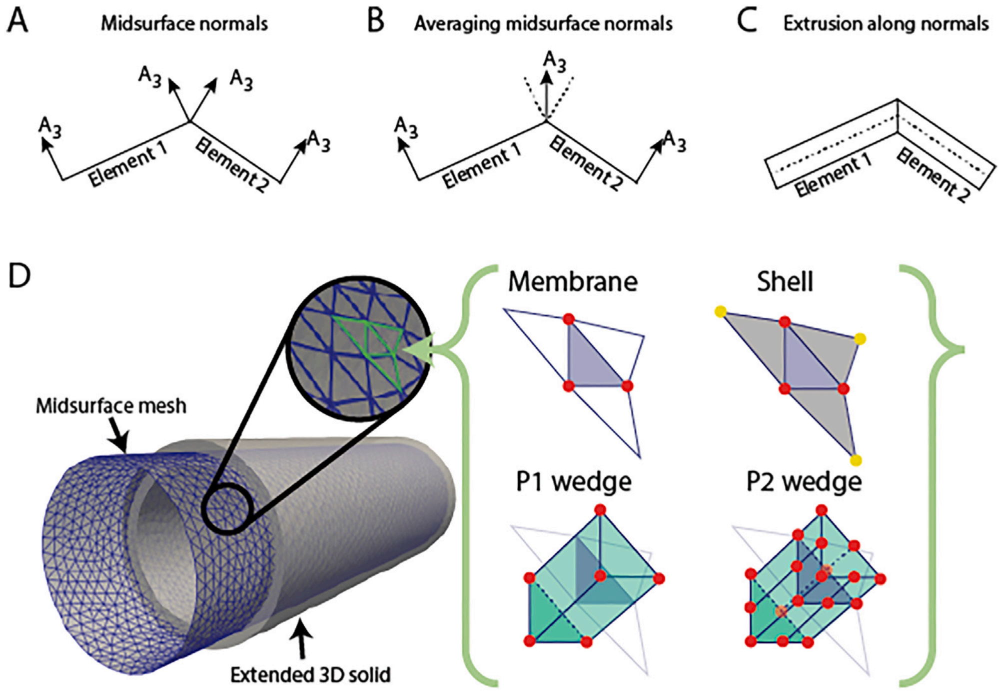

Fig. 2. (A–C) Generation of a solid mesh using extrusion of the midsurface mesh. (D) Extension of the midsurface mesh of a cylinder to generate a 3D solid cylindrical geometry. The resulting solid geometry has been clipped to reveal the initial midsurface mesh. The nodes per element for each formulation are denoted by solid red circles. The yellow circles represent the nodes in the neighboring patch of the nonlinear shell.

2.3 Discretization

To compare the performance of different formulations under the closest possible conditions, we chose a particular finite element discretization for the continuum formulation. Specifically, the solid mesh consists of wedge (or triangular prismatic) elements (Zienkiewicz et al., 2005) generated by performing an extension of the midsurface triangular elements used for the membrane and shell formulations. This approach ensures that the midsurface discretization remains identical for all formulations. An additional advantage of this construction is that the midsurface, inner surface, and outer surface of the 3D model share the same mesh topology, thereby minimizing mesh-induced differences when comparing results between the 2D and 3D formulations. In this way, differences observed in the simulations can be more directly attributed to the formulation itself rather than to discrepancies in the mesh discretization. Finally, we anticipate future implementations in fluid–solid-interaction (FSI) and fluid–solid-growth (FSG) formulations, which often use tetrahedral elements for the fluid domain. Discretization comprises three steps: (1) Computation of the normal vector in the undeformed configuration $\boldsymbol{A}_3$ at each node within every element, (2) Generation of a continuous distribution of $\boldsymbol{A}_3$ across elements by local averaging, and (3) Extension of triangular elements along the continuous normal vectors $\boldsymbol{A}_3$, both inwards and outwards of the midsurface. This process is summarized in Fig. 2(A–C). Fig. 2 (D) shows results of this extrusion strategy applied on a midsurface mesh of a cylinder to generate a solid cylindrical geometry. Here, the resulting solid geometry has been clipped to reveal the initial midsurface mesh.

We consider two different implementations for the 3D solid model. The first implementation, referred to as P1 wedge, utilizes linear interpolation both in-plane and through-the-thickness, while the second implementation utilizes quadratic interpolation both in-plane and through-the-thickness, and is referred to as P2 wedge. The difference in interpolation order results in a different number of degrees of freedom per element. Specifically, both the membrane and the (rotation free) shell formulations employ linear triangular elements to represent the midsurface plane, resulting in 9 degrees of freedom per element. In contrast, the P1 wedge formulation employs a linear wedge element with six nodes, which results in 18 degrees of freedom per element. Lastly, the P2 wedge formulation employs a quadratic interpolation of displacement both in-plane and through-the-thickness, resulting in 54 degrees of freedom per element (see Fig. 2(D)).

3 Results

The performance of the different formulations is demonstrated in three different geometries (see Table 1): a cylindrical geometry, an idealized arterial bifurcation model comprising a main artery and an orthogonal side branch, and a mouse-specific aortic model featuring three branches from the arch. Similarly, in terms of material properties, the first example represents the simplest case with uniform material properties and wall thickness. The second example employs uniform material properties with regionally varying wall thickness. The third example considers subject-specific, regionally-varying values for both material properties and wall thickness. In addition, the second case employs uniform external tissue support, while the third example uses regionally-varying values. These examples have been carefully chosen to introduce increasing degrees of complexity, both in terms of the geometry and material properties. In addition, a rigorous analysis of convergence rates, relying on analytical solutions for axisymmetric and plate geometries, is presented in Section 3.1. The effect of axial prestretch (i.e., restoration of the *in vivo* value of axial stretch, which arises due to somatic growth, prior to pressurization) is also studied on the cylindrical geometry in Section 3.2.1.

The different formulations were implemented using different programming languages across different platforms (namely, FORTRAN for the membrane and shell formulations, and MATLAB for the 3D formulations) and simulations were performed using different computers, hence a direct comparison of the wall clock time is meaningless. Therefore, the total number of degrees of freedom serves as a metric for their relative computational costs. It is also noted that, in the present study, both the 2D and 3D formulation solvers were executed in a single-core (serial) setting. As a result, no domain decomposition or inter-process

Table 1
Schematic illustration of the three geometries and respective modeling choices compared in this work: a cylindrical geometry, an idealized bifurcation model comprising a main artery and an orthogonal side branch, and a mouse-specific aortic model featuring multiple branches.

	Cylinder	Bifurcation	Mouse-specific
Geometry	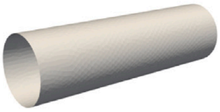	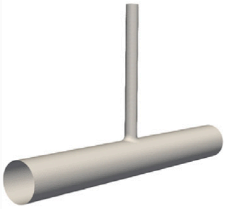	
Material model	Four-fiber	Four-fiber	Four-fiber
Regionally Varying Thickness	No	Yes	Yes
Regionally Varying Properties	No	No	Yes
External Tissue Support	No	Yes	Yes

Table 2
Degrees of freedom for each geometry for different formulations.

Geometry	Membrane	Shell	P1 wedge	P2 wedge
Cylinder	8601	8601	17,202	102,420
Bifurcation	–	48,945	97,890	586,134
Mouse-specific	–	63,843	127,686	764,865

communication was involved, and all element neighborhoods required for the shell formulation were locally available. Noting this, Table 2 lists the resulting number of degrees of freedom for each geometry for different formulations. The degrees of freedom for each geometry and model were determined from mesh-independence studies.

3.1 Convergence rate

A convergence analysis was performed to assess the impact of mesh refinement on the results obtained from the different formulations. Two alternative canonical problems are selected to demonstrate the expected orders of convergence of each formulation before establishing comparisons for a common problem of interest : **(1)** a thin plate with 10 mm × 10 mm × 0.43 mm dimensions for the 3D formulations (P1 and P2 wedge), and **(2)** a cylindrical tube with midsurface radius R = 8.6 mm, axial length L = 60 mm, and thickness-to-radius ratio H/R = 0.25 for the 2D formulations (membrane and rotation-free shell). Meshes for both geometries are refined only in the in-plane direction. This choice ensures a fair comparison among the different models. The error is calculated as the L2 norm of the discrepancy between the simulation results and the analytical solutions. The analytical solution of the thin plate problem is described in Appendix A. The axisymmetric solution described in Section 3.2 is used for the analytical solution of the cylindrical tube.

Fig. 3 shows results of the convergence analysis on displacement and stress. 3D formulations exhibit second- and third-order convergence rates in displacement for the P1 and P2 wedge, respectively. For stress, first- and second-order convergence rates were obtained for the P1 and P2 wedge, respectively. These are expected convergence rates for linear and quadratic interpolations. Both membrane and rotation-free shell formulations showed near second-order convergence rates for displacement. These convergence rates are consistent with previous studies using a rotation-free shell formulation (Behzadinasab et al., 2022). As for the stress field, both membrane and shell formulations demonstrated near-second order convergence rates (1.88 and 1.87, respectively).

3.2 Cylindrical geometry

3.2.1 Effects of wall thickness

First, we compare the performance of different formulations against the well-known axisymmetric solution for a cylindrical tube. Details of this solution can be found elsewhere (Holzapfel et al., 2000; Humphrey, 2013). This solution provides, in the most general case, the static mechanical response of a thick axisymmetric tube under combined distension and extension. We consider a cylindrical tube with midsurface radius R = 8.6 mm and axial length L = 60 mm. To assess the performance of different formulations for increasing wall thickness-to-radius ratio, we consider different biomechanics-focused values of H/R = 0.05, 0.10, 0.15, 0.20 and 0.25 while keeping the undeformed midsurface radius the same. The wall is characterized by a four-fiber family model with the material parameters listed in Appendix Table B.1. For the purpose of this example, the tube is subjected to an internal pressure that is increased linearly from 0 mmHg to 80 mmHg (10.66 kPa) while the ends of the tube are held fixed at an axial stretch of 1.0 (the effect of axial stretch greater than 1.0 is studied in Section 3.2.2.) while allowing changes in the radial direction. The comparison is performed in the mid-plane slice along the axial direction. The axisymmetric solution is taken to be the true solution and is compared against the solutions obtained from four different implementations: membrane, shell, P1 wedge, and P2 wedge.

Fig. 4(A–E) shows the cross section of the cylindrical tube for the five different thickness-to-radius ratios considered. Fig. 4(F–T) presents plots of the following three quantities of interest versus pressure: midsurface radius (Fig. 4(F–J)), first invariant of Green–Lagrange strain tensor (Fig. 4(K–O)), and circumferential Cauchy stress (Fig. 4(P–T)). For H/R = 0.05, all four models yield good agreement with the axisymmetric solution. 2D formulations approach better the axisymmetric solution than the 3D formulations with maximum differences of 1.38%, 1.08%, 2.59%, and 2.2% for the membrane, shell, P1 wedge, and P2

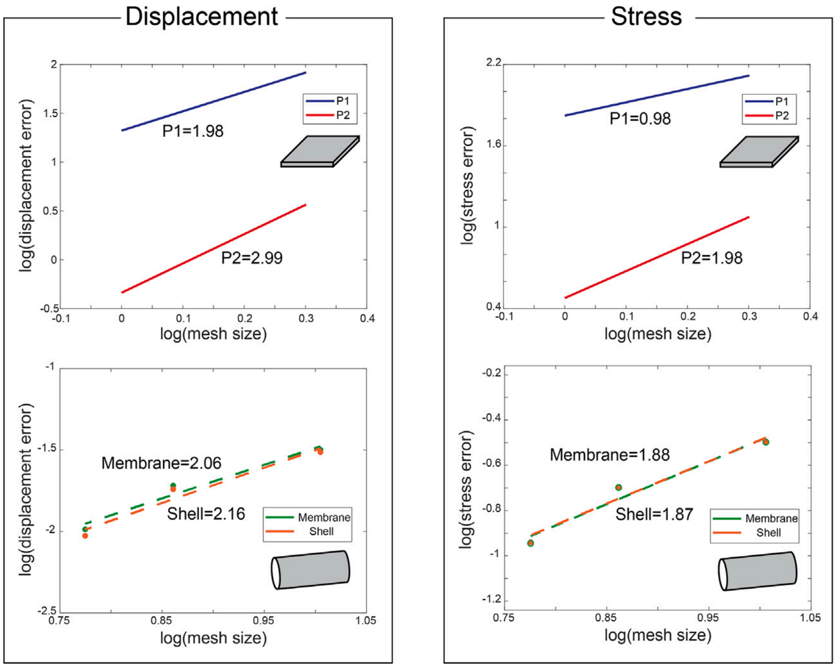

Fig. 3. Convergence analysis results for displacement and stress. Plots are log scale and contain slopes of each formulation's trend lines.

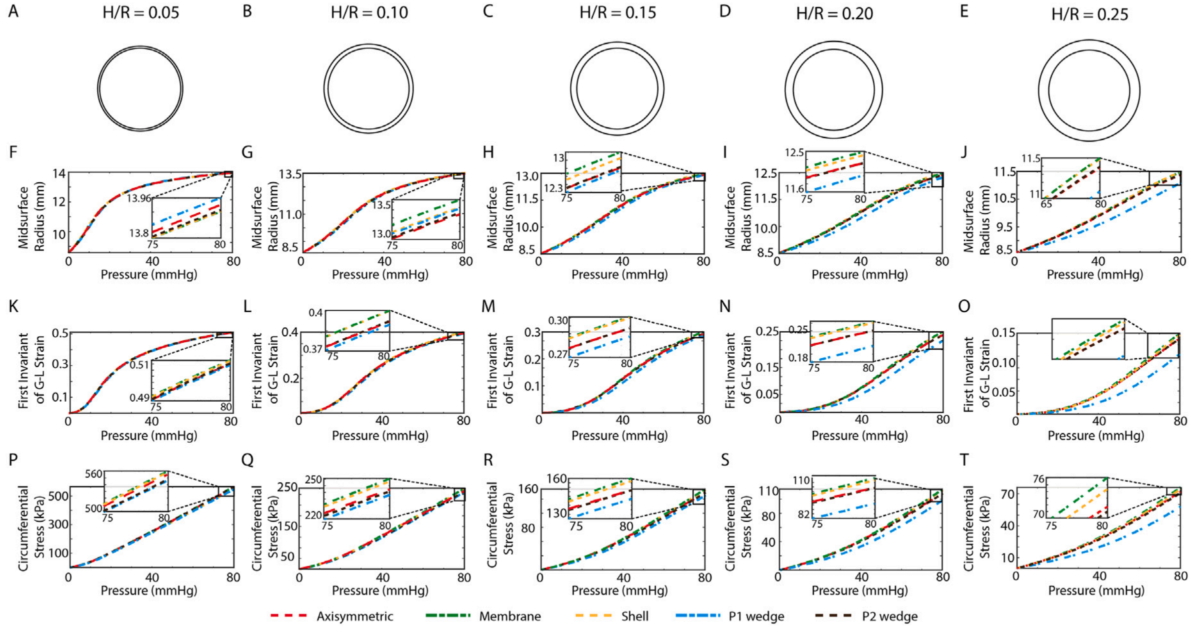

Fig. 4. (A–E) Cross-sections of the cylindrical tube for three different thickness-to-radius ratios. (F–J), (K–O), and (P–T) compare the values of midsurface radius, first invariant of Green–Lagrange strain tensor, and circumferential Cauchy stress, respectively, as a function of pressure for all formulations against the axisymmetric solution.

wedge implementations, respectively. As the wall thickness increased, differences between the membrane, shell, and P1 wedge and the axisymmetric solution became more pronounced. The P1 wedge was more sensitive to changes in the thickness-to-radius ratio than the membrane and shell. The P2 wedge yielded good agreement with the axisymmetric solution for all thicknesses. For $H/R = 0.25$, the P1 wedge solution yielded 10.67% smaller displacement, 20.8% lower first invariant of Green–Lagrange strain tensor, and 19.2% lower circumferential stress, compared to the axisymmetric solution. Membrane and shell solutions exhibited smaller deviations from the axisymmetric solution, with maximum differences for displacement of 6.4% and 4.6%, respectively. The P2 wedge solution yielded the best agreement with the axisymmetric solution, with a maximum displacement difference of 1%.

Note that all the numerical formulations employed an unstructured, non-axisymmetric mesh that might have introduced differences from the axisymmetric solution. Nonetheless, these results indicate that the 2D formulations (membrane and shell) perform better than the linear continuum formulation (P1 wedge) for the same surface mesh as the wall thickness increased. This is an interesting finding, given that the P1 wedge solution was obtained with twice the number of degrees of freedom compared to the 2D formulations. In contrast, the P2 wedge formulation, using the highest number of degrees of freedom, yielded

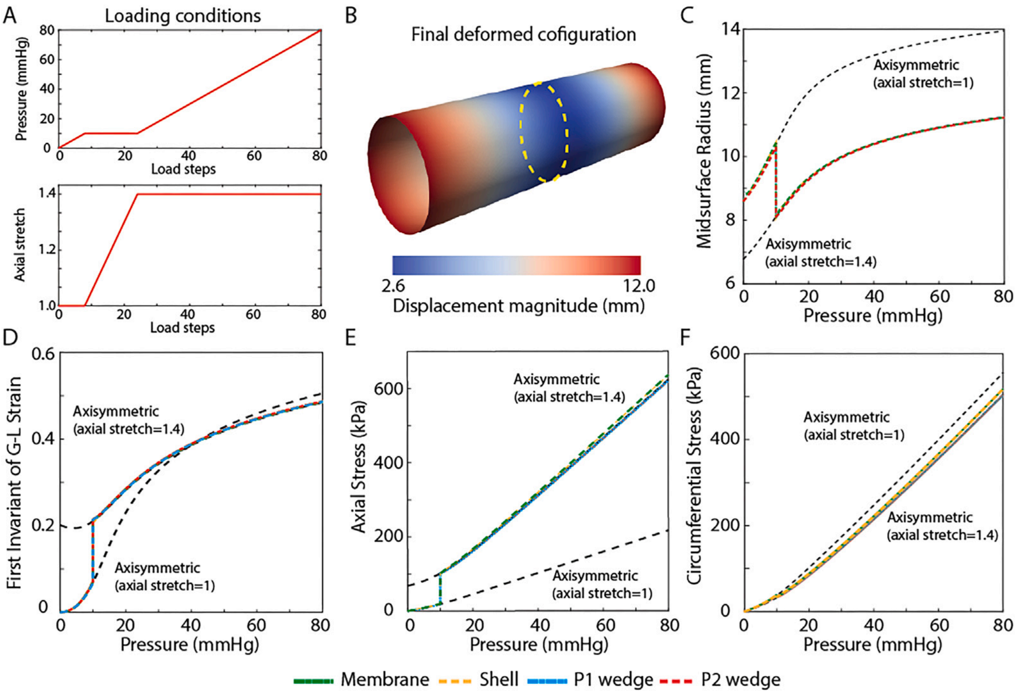

Fig. 5. Axial pre-stretch and pressurization of a cylindrical tube. (A) Step-wise loading imposed during the computations. (B) Final P2 deformed configuration at 80 mmHg; the yellow ring shows the mid-plane slice along the axial direction where panels C–F are calculated. (C–F) Compare values of midsurface radius, first invariant of Green–Lagrange strain tensor, and axial and circumferential Cauchy stress, respectively, with pressure for all formulations against the axisymmetric solution.

the best agreement with the axisymmetric solution, except for the thinnest geometry ($H/R = 0.05$). This observation also suggests that the discrepancies observed for the P1 wedge formulation are primarily related to the interpolation accuracy of the element rather than mesh-induced effects. In particular, the results obtained with the P2 wedge formulation closely match those of the 2D shell formulation and show significantly improved agreement with the axisymmetric reference solution. If mesh-induced errors were the dominant source of discrepancy, comparable deviations would be expected for both the P1 and P2 wedge formulations, since they share the same underlying surface discretization. Instead, the improved performance of the higher-order P2 wedge formulation indicates that the differences mainly arise from the limited interpolation capability of the linear P1 wedge element.

3.2.2 *Effects of axial pre-stretch*

Axial stretch (“pre-stretch”) arises in arteries during development (Dobrin et al., 1975; Cardamone et al., 2009), then decreases with aging as well as with diverse disease conditions. In healthy young adults, axial stretch differs from artery-to-artery within the same species and differs within the same artery across species. It is not our intent here to explore pre-stretch as a function of arterial location, age, disease status, or species, but rather to examine the ability of the four different formulations to capture associated changes in stress. Hence, in this study, an extension-stretch loading scenario is used to analyze the effect of pre-stretch. We use the cylindrical geometry from Section 3.2 with thickness-to-radius ratio of 0.05. The axisymmetric solutions with axial stretch of 1.0 and 1.4 are taken to be the true solution. Fig. 5(A) shows the loading condition: pressurization to 10 mmHg (1.33 kPa), followed by an extension to an axial stretch of 1.4 at constant pressure, and a subsequent pressurization to 80 mmHg (10.66 kPa). During the entire loading condition, both ends of the cylinder are allowed to move in the radial direction (radial rollers). The same four-fiber family model and material parameters in Section 3.2 are used.

Fig. 5(B) shows the deformed configuration obtained using the P2 wedge formulation at 80 mmHg (10.66 kPa) pressure and a 1.4 axial stretch. Fig. 5(C–F) presents plots of four different quantities of interest (C: midsurface radius, D: first invariant of Green–Lagrange strain tensor, E: axial Cauchy stress, and F: circumferential Cauchy stress) versus pressure at the mid-plane slice (yellow dotted ring in Fig. 5(B)). All four models yield good agreement with the axisymmetric solution. For the midsurface radius and the first invariant of Green–Lagrange strain tensor, the largest error for all four formulations is less than 1%. For the axial and circumferential Cauchy stress, 2D formulations yield 2% higher stresses than the axisymmetric and 3D formulations. As we found that all four formulations are able to cope with axial pre-stretch, we used fixed ends boundary condition for next two examples. Note, too, the technique used to impose axial pre-stretch is not restricted to cylindrical geometries and can, in principle, be applied to arbitrary geometries.

3.3 *Idealized bifurcation geometry*

Next, consider an idealized bifurcation model comprising a main artery and a side branch. The main vessel is a cylinder with radius 0.6 mm, while the side branch is a cylinder with radius 0.2 mm. To avoid a sharp intersection, the two branches are blended via a fillet with radius 0.2 mm. We refer to the region surrounding the intersection of the two branches as the ‘blend region’. Wall thickness is taken to be 10% of the local radius, resulting in a wall thickness of 0.06 mm and 0.02 mm for the main vessel and the branch, respectively, with a smooth variation of thickness in the blend region. Therefore, this example introduces two additional geometrical complexities compared to the cylindrical geometry: (a) a bifurcation region due to the presence of a side branch and (b) regionally varying thickness due to different thickness of the main artery and the side branch. We use a four-fiber material model for the vessel wall with the same material parameters used in Section 3.2. In this example, we use homogeneous material parameters for the entire vessel surface. We linearly pressurize this geometry from 0 mmHg to 80 mmHg (10.66 kPa) with fixed end boundary conditions. As illustrated in our prior work (Nama et al., 2020), it is crucial to include the effect of surrounding tissue via external support boundary conditions to avoid non-physiological deformations and buckling of the arterial wall (which is expected to be greater in cases of no axial pre-stretch, hence the lack of pre-stretch in this numerical example provides a stringent test of the perivascular support). Specially, we modeled the effect of external tissue via an imposed traction on the outer wall, $\boldsymbol{\sigma}\mathbf{a}_3 = -k_s\mathbf{u}$, where $\mathbf{a}_3$, k_s, and $\mathbf{u}$ are unit normal vector, the coefficient associated with simplified elastic response of the external tissue, and displacement vector. For the current example, we use $k_s = 10^5\ \mathrm{g/(mm^2\ s^2)}$. The isotropic mesh size is taken to be 0.06 mm for the main vessel, 0.04 mm for the side branch, and 0.01 mm for the blend region. The reduced mesh size for the blend region aids convergence. The membrane formulation failed to converge for this example, as expected, due to its inability to handle bending mode deformations in the blend region. Consequently, the comparison for this case is performed only among shell, P1 wedge, and P2 wedge formulations.

Fig. 6(A) shows the displacement magnitude in the final deformed configuration, obtained using the P2 wedge formulation, with maximum displacement observed near the bifurcation. Fig. 6(I) compares the final deformed configuration in plane I, obtained using shell, P1 wedge, and P2 wedge formulations. Fig. 6(I) also includes the corresponding unloaded configuration to indicate the extent of deformation. The shell formulation shows a good agreement with the P2 wedge formulation. This result shows that the shell formulation matches wedge formulations well in the blend region of the bifurcation. Fig. 6(II) and (III) compare solutions from different formulations at location II and III in Fig. 6(A), respectively. We plot the values of three different quantities as a function of pressure: midsurface radius, first invariant of Green–Lagrange strain tensor, and circumferential Cauchy stress. These plots show that the solutions from the shell formulation match well with P2 wedge at both locations II and III. The maximum difference between the shell and P2 wedge formulations in location II are 0.4, 5.8, and 2.3% for midsurface radius, first invariant of Green–Lagrange strain tensor, and circumferential Cauchy stress, respectively. The maximum difference between the shell and P2 wedge formulations in location III are 0.4, 2.4, and 3.4% for midsurface radius, first invariant of Green–Lagrange strain tensor, and circumferential Cauchy stress, respectively.

This analysis revealed two significant findings: (1) The membrane formulation is unsuitable for general biomechanical analysis due to its inability to handle bending mode deformation in geometries with branches, (2) The shell formulation yields a good agreement with the P2 wedge formulation, despite using only 8.4% of the degrees of freedom (see Table 2).

3.4 *Mouse-specific geometry*

Next, we compare the different formulations in a mouse-specific anatomy featuring three upper branches off the aortic arch, which necessarily introduces marked curvature as well. The anatomy was obtained via non-invasive *in vivo* micro-CT and has been employed in our previous work (Cuomo et al., 2019). We model the aortic wall using a four-fiber family material model with regionally varying material parameters and wall thickness distribution determined from experimental data (See Appendix Table B.2). The external tissue support boundary condition with $k_s = 1.2{\times}10^5\ \mathrm{g/(mm^2\ s^2)}$ and $k_s = 3.0{\times}10^5\ \mathrm{g/(mm^2\ s^2)}$ are used for the main aorta and side vessels to prevent non-physiological deformations and buckling of the arterial wall. These values are initially selected based on physiologically motivated values reported in our previous work (Cuomo et al., 2019). Starting from these baseline values, the external tissue support value was subsequently increased as needed to suppress non-physical wrinkling artifacts, particularly those observed in the P2 wedge formulation. This calibration was performed to ensure numerical stability and a fair comparison across formulations, rather than to represent a specific surrounding tissue stiffness (see Appendix D). Referring to Table 1, this example introduces several additional complexities compared to previous examples by considering regional variations of material properties and wall thickness as well as the external tissue support. We subject this aortic geometry to an internal pressure that is increased linearly from 0 mmHg to 80 mmHg $(10.66$ kPa$)$ with fixed end boundary conditions.

Fig. 7(A) shows the volume rendered geometric model and associated skeleton, obtained from the micro-CT data for a 20-week old wild-type mouse. Fig. 7(B) shows displacement magnitude in the final deformed configuration obtained using the shell formulation. Panels I, II, and III in Fig. 7(C) compare the final deformed midsurface configuration obtained using different formulations at locations I, II, and III in Fig. 7(B), respectively. The corresponding unloaded configuration of the midsurface has also been included to indicate the extent of deformation during the pressurization. The deformed configuration predicted by both the shell and P1 wedge formulation agreed well with the P2 wedge formulation at all three locations. Panel III of Fig. 7(C) shows that the deformation at the blend and side vessel is lower than the main aorta due to the large external tissue support value. This result also demonstrates that the shell formulation matches the 3D wedge formulations well in the blend region of the subject-specific geometry.

Next, we compared shell, P1, and P2 formulations in terms of various kinematic quantities at the locations I and II indicated in Fig. 7(B). We plot values of three different metrics: midsurface displacement, first invariant of Green–Lagrange strain tensor, and circumferential Cauchy stress with pressure, at locations I (mid row) and II (bottom row). The maximum difference between the shell and P2 wedge formulations in location I (main aorta) are $0.3, 3.1$, and 3.7% for midsurface radius, first invariant of Green–Lagrange strain tensor, and circumferential Cauchy stress, respectively. The maximum difference between the shell and P2 wedge formulations in location II (smallest side vessel) are $0.5, 9.8$, and 7.4% for midsurface radius, first invariant of Green–Lagrange strain tensor, and circumferential Cauchy stress, respectively. These results show that the differences are greater with the smaller vessel than the main aorta. Nonetheless, despite this discrepancy, the results from all formulations agree reasonably well.

Overall, given that the shell formulation uses only 16.7% and 8.4% of the degrees of freedom used for the P1 wedge and P2 wedge formulation, respectively, (see Table 2) our results suggest that the shell formulation represents a computationally superior alternative, considering a balance between cost and accuracy, to the 3D wedge formulations. We also found that the shell formulation is less sensitive to buckling than the 3D wedge formulations. Finally, as noted in Introduction, the shell formulation offers another advantage over 3D models by avoiding the need for creating an extended mesh from the medical imaging data.

4 Discussion and conclusions

We compared three different nonlinear formulations for vascular biosolid mechanics; moreover, for the 3D solid formulation, we considered two different implementations employing wedge elements with linear and quadratic interpolation, referred to as P1 wedge and P2 formulations, respectively. We compared results in three geometries having increasing degrees of complexity: (a) a cylindrical model, (b) an idealized bifurcation model comprising a main artery and a side branch, and (c) a mouse-specific arterial model featuring three branches. To ensure fair comparisons, the solid mesh was generated via an extension of the triangular mesh elements used for 2D formulations to obtain wedge (or triangular prismatic) elements.

An important consideration for 3D formulations is their ability to satisfy the incompressibility condition, through a penalty parameter λ in the volumetric term $U(J)$ see Eq. (52). To study the impact of this parameter, a sensitivity analysis was conducted for both P1 and P2 wedge formulations. Details of this sensitivity analysis are given in Appendix C.

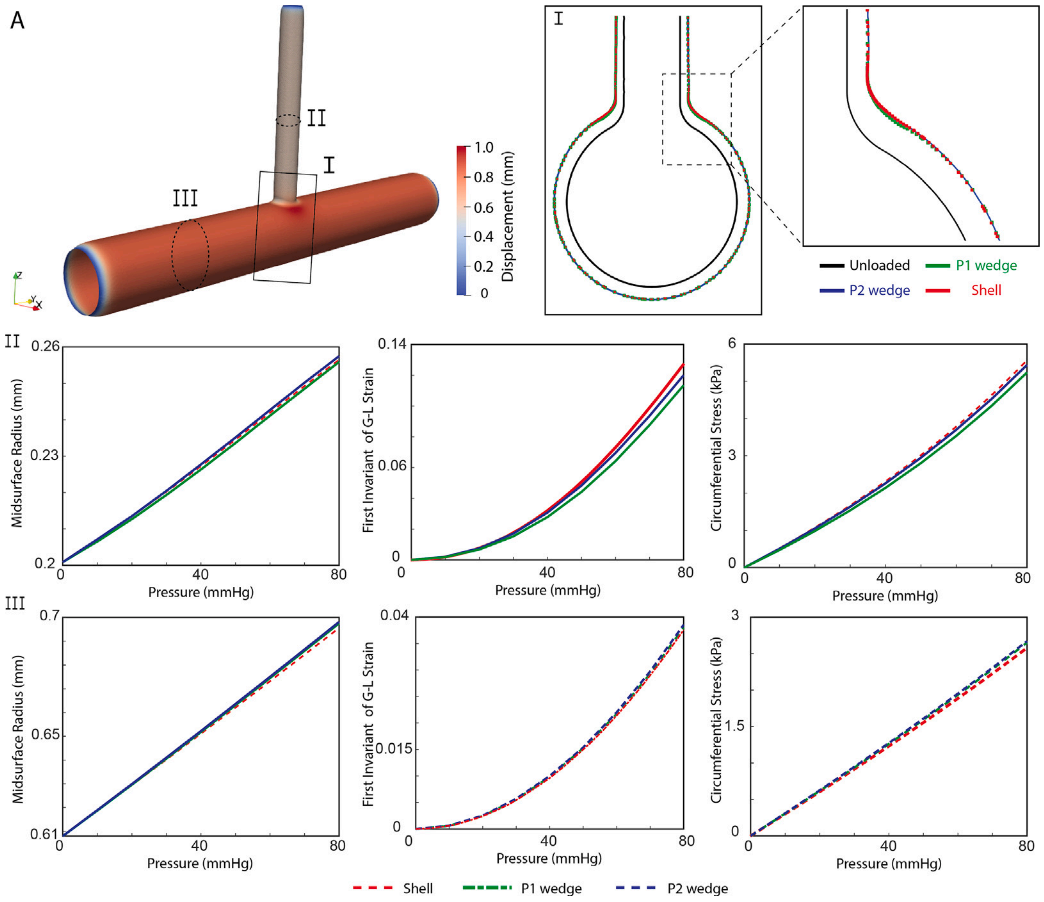

Fig. 6. Comparison of shell, P1 wedge, and P2 wedge formulations for an idealized bifurcation geometry. (I) shows the unloaded and final configuration from the shell, P1 wedge, and P2 wedge formulations. (II) and (III) compare values of midsurface radius, first invariant of Green–Lagrange strain tensor, circumferential Cauchy stress with pressure for two different locations.

For the cylindrical geometry, we compared the solution from the four implementations against the well-known axisymmetric solution for five different thickness-to-radius ratios. For the thin wall case ($H/R = 0.05$), all formulations agreed well with the axisymmetric solution; 2D formulations performed slightly better than the 3D formulations with maximum errors of 1.38%, 1.08%, 2.59%, and 2.2% for the membrane, shell, P1 wedge, and P2 wedge implementations, respectively. However, as wall thickness increased relative to radius ($H/R = 0.25$), the P1 wedge solution deviated significantly from the axisymmetric solution. The membrane and the shell formulations outperformed the P1 wedge solution and yielded results within 6.4% and 4.6%, respectively, of the axisymmetric solution. The P2 wedge formulation provided the best agreement with the axisymmetric solution, with errors less than 1%. Important considerations for the thinnest tissue scenario ($H/R = 0.05$): (1) P2 is not necessarily the best formulation because it fails to ensure incompressibility exactly unless a mixed Lagrange multiplier approach is pursued (Bonet et al., 2016) and it may introduce instability across the thickness (Poya et al., 2016, 2023), and (2) the shell outperforms the membrane, which is known to be unstable in the presence of wrinkling (Lu et al., 2001), and (3) P1 is inaccurate and shows potential risk of locking (see Appendix C) despite using twice the number of degrees of freedom.

Next, we compared results from different formulations in an idealized bifurcation model comprising a main artery and a side branch, with regionally varying wall thickness. The membrane formulation failed to converge for this example due its inability to handle bending mode deformations in geometries with branches. This observation indicates that a nonlinear membrane formulation is inappropriate for general vascular biomechanical analyses of complex geometries that routinely feature vessel bifurcations. Among the remaining formulations (shell, P1 wedge, and P2 wedge), the shell solution captured the P2 wedge solution with good accuracy (maximum error of 6%) as well as the P1 wedge solution (maximum error of 4.5%). Again, these results point to the effectiveness of shell formulations for vascular biomechanics, given that it requires only 17% and 8.4% of the degrees of freedom for P1 wedge and P2 wedge formulations, respectively.

Lastly, we compared results from the shell, P1 wedge, and P2 wedge formulations for a mouse-specific arterial model featuring three branches, while incorporating regional variations of material properties and wall thickness as well as external tissue support. Results from the different formulations agreed reasonably well, with the shell solutions yielding maximum differences of only 7.4% relative to the P2 wedge solution. Given that the shell formulation employs 8.4% degrees of freedom than the P2 wedge formulations (see Table 2), these results again highlight the efficacy of shell formulations, considering a balance between cost and accuracy. These results also suggest an additional practical advantage of the 2D shell formulation: because it involves substantially fewer degrees of freedom, the need for parallel implementation is less critical than for the 3D wedge formulations.

One limitation of the present study is the absence of a multilayer representation of the arterial wall. The aortic wall is composed of three primary layers — intima, media, and adventitia — each with distinct micro-structural constituents and mechanical properties that influence the overall mechanical response of the vessel (Humphrey, 2013; Holzapfel et al., 2004; de Lucio et al., 2021; Giudici and Spronck, 2022; Von Maltzahn et al., 1981; Demiray and Vito, 1991). Previous studies have shown that explicitly accounting for these layers can significantly affect stress distributions, stiffness, and deformation behavior

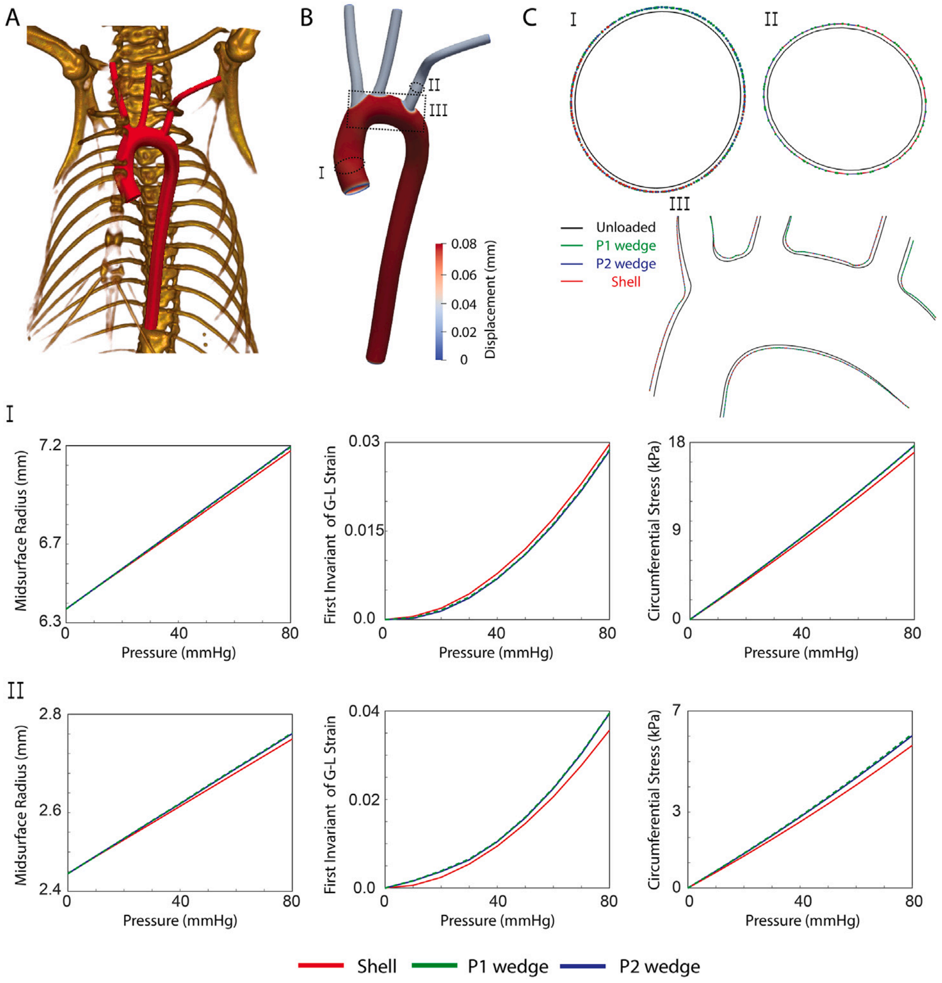

Fig. 7. Comparison of shell, P1 wedge, and P2 wedge formulations for a mouse-specific geometry. (A) Volume rendered geometric model of the aortic anatomy of a 20-week old wild-type female mouse. (B) Plot of the final deformed configuration obtained via the shell formulation. (c) Enlarged cross-sections comparing the deformed configurations predicted by three formulations at locations I, II, and III. Middle (I) and bottom (II) row plots compare values of midsurface radius, first invariant of Green–Lagrange strain tensor, circumferential Cauchy stress as a function of pressure.

of arterial tissues. For example, Diaz et al. incorporated multilayer constitutive descriptions to investigate layer-specific mechanics and stress distributions in arteries (Diaz et al., 2021). Similarly, Holzapfel and Ogden used multilayer 3D solid models to examine the mechanical behavior of human aorta and to analyze the contribution of individual layers to the overall wall mechanics (Holzapfel and Ogden, 2010). In such models, 3D solid formulations naturally allow the arterial wall thickness to be discretized into multiple layers, each assigned its own constitutive properties. In contrast, representing multilayer behavior in 2D formulations such as membrane or shell models is less straightforward, as these formulations describe the wall using a single midsurface and may therefore require additional assumptions, such as homogenization of the layer properties or specialized shell formulations with layer-wise integration. By contrast, homogenized representations of the arterial wall can be sufficient in studies of FSI wherein it is the overall effect of the wall mechanics on the hemodynamics that is most important and similarly for certain FSG implementations. As is always the case, the choice of material model depends on the application of interest. Herein, we did not include a multilayered representation of the wall given our expressed goal of comparing results across membrane, shell, and 3D formulations.

Another potential limitation of this study is the absence of residual stress in the formulations. Residual stresses (in radial, circumferential, and axial directions) appear to arise *in vivo* during development but, by definition, exist in the absence of applied loads and can be inferred experimentally from *in vitro* tests on excised vessels. These stresses thus differ from so-called pre-stresses (also in radial, circumferential, and axial directions), which arise both from somatic growth and pressurization of the *in vivo* computational configuration. Residual stresses were discovered in the early 1980s and shown soon thereafter to homogenize the calculated transmural distribution of wall stress in healthy adult vessels (Humphrey, 2013). For this reason, approaches that yield radially averaged values of wall stress (including membrane and shell models) can represent well the actual state of stress in certain cases, though with the need for care in bi-layered models of the arterial wall in which the medial and adventitial layers may exhibit separate near homogeneous distributions of wall stress (Bellini et al., 2014). There remains a pressing need, however, to evaluate experimentally how residual stresses change with aging, disease progression, and even clinical intervention, with the expectation that changing residual stresses will need to be modeled explicitly in these many cases. There is also a need to understand better how these residual stresses vary from site-to-site in complex vascular geometries and how to prescribe or account for these stresses computationally in complex cases. Residual stresses were not included explicitly herein to enable the most direct comparison across the four formulations and because we only considered cases that did not include disease.

In this study, external tissue support is implemented to avoid non physiological deformations, including wrinkling and buckling of the arterial wall, especially for the 3D wedge formulations. The external tissue support acts on the outer surface of the vessel wall in 3D formulations, while it acts on the wall midsurface in the shell formulation. From a practical perspective, this implies that the choice of external tissue support parameters must be formulation-specific, to match the dynamic deformation data, if available.

Overall, our results indicate that shell formulations represent an effective compromise between computational cost and accuracy for vascular biomechanics. The membrane formulation may still provide a reasonable approximation for idealized vascular problems or simple thin biological structures, such as leaflets in valves, where bending effects are negligible. However, for anatomically realistic geometries involving branches or strong curvature variations, formulations that include bending stiffness, such as shell or 3D solid models, are more appropriate. Furthermore, given the lack of rotational degrees of freedom, the shell formulation is ideally-suited to serve as the structural model in fluid–structure interaction frameworks and fluid–solid-growth models for vascular biomechanics. We are currently utilizing the shell formulation to develop a strongly coupled, monolithic, computationally efficient, nonlinear fluid–structure interaction framework in the open-source software CRIMSON (Arthurs et al., 2021) via an adaption of the Coupled Momentum Method (Figueroa et al., 2006) that accounts for large displacements and nonlinear material models. Given the computational efficiency and accuracy of the shell formulation, this framework promises to provide a computationally efficient, yet accurate, alternative to the current fluid–structure interaction formulations that employ a 3D representation of the vessel wall (Bathe and Kamm, 1999; Hron and Mádlík, 2007).

CRediT authorship contribution statement

Taeouk Kim: Writing – review & editing, Writing – original draft, Visualization, Methodology, Investigation, Formal analysis, Data curation. **Rogelio Ortigosa:** Writing – review & editing, Writing – original draft, Resources, Methodology, Investigation, Funding acquisition, Formal analysis, Data curation, Conceptualization. **Nitesh Nama:** Writing – review & editing, Writing – original draft, Methodology, Funding acquisition, Formal analysis, Data curation, Conceptualization. **Miquel Aguirre:** Writing – review & editing, Methodology, Funding acquisition, Formal analysis, Data curation. **Antonio J. Gil:** Writing – review & editing, Resources, Methodology, Funding acquisition, Data curation, Conceptualization. **Jay D. Humphrey:** Writing – review & editing, Supervision, Project administration, Investigation, Funding acquisition, Conceptualization. **C. Alberto Figueroa:** Writing – review & editing, Writing – original draft, Supervision, Resources, Project administration, Methodology, Investigation, Funding acquisition, Conceptualization.

Declaration of competing interest

The authors declare that they have no known competing financial interests or personal relationships that could have appeared to influence the work reported in this paper.

Acknowledgments

C.A. Figueroa acknowledges the support from National Institutes of Health, United States (R01-HL158723 and U01HL135842) and by the Edward B. Diethrich M.D. Professorship. Furthermore, Dr. Figueroa acknowledges (R01 HL105297) with J.D. Humphrey. N. Nama acknowledges the support from the American Heart Association, United States (23CDA1048343). R. Ortigosa acknowledges support of grant PID2022-141957OA-C22 funded by MICIU/AEI/10.13039/501100011033 and by ERDF A way of making Europe, and also the support of grant 21996/PI/22 funded by Fundacion Seneca - Agencia de Ciencia y Tecnologia de la Region de Murcia. M. Aguirre acknowledges the support of Grant PID2022-136668OA-I00 funded by MCIN/AEI/10.13039/501100011033 and by ERDF A way of making Europe, and by grant RYC2023-042592-I funded by MICIU/AEI/10.13039/501100011033 and by ESF+. A.J. Gil acknowledges the support of The UK Leverhulme Trust through a Leverhulme Fellowship.

Appendix A. Analytical solution of the thin plate problem

In this section, we demonstrate the $p-$order of accuracy of the wedge finite element formulations as a function of the finite element approximation space. Towards that goal, an *ad-hoc* test problem is constructed (Ortigosa et al., 2016) such that a smooth solution is guaranteed. The following displacement field $\boldsymbol{u}^{\text{exact}}$ is considered

$$\boldsymbol{u}^{\text{exact}} = \begin{bmatrix} AX_1^3 & BX_2^3 & CX_3^3 + X_1^3 \end{bmatrix}^T \tag{A.1}$$

with $A = 1.2$, $B = 1.3$, $C = 1.5$. The corresponding deformation gradient tensor is

$$\boldsymbol{F}^{\text{exact}} = \frac{\partial \boldsymbol{x}}{\partial \boldsymbol{X}}^{\text{exact}} = \frac{\partial\left(\boldsymbol{u}^{\text{exact}} + \boldsymbol{X}\right)}{\partial \boldsymbol{X}} = \begin{bmatrix} 1+3AX_1^2 & 0 & 0 \\ 0 & 1+3BX_2^2 & 0 \\ 3X_1^2 & 0 & 1+3CX_3^2 \end{bmatrix} \tag{A.2}$$

We consider the following Neo-Hookean strain energy density,

$$W = \frac{\mu}{2}(\boldsymbol{F} : \boldsymbol{F}) - \mu \log \det \boldsymbol{F} \tag{A.3}$$

with $\mu = 1$. The corresponding first Piola–Kirchhoff stress tensor is

$$\boldsymbol{P}^{\text{exact}} = \left.\frac{\partial W}{\partial \boldsymbol{F}}\right|_{\boldsymbol{F}^{\text{exact}}} = \mu \boldsymbol{F}^{\text{exact}} - \frac{\mu}{\det \boldsymbol{F}^{\text{exact}}} \boldsymbol{H}^{\text{exact}} \tag{A.4}$$

where $\boldsymbol{H} = (\det \boldsymbol{F})\ \boldsymbol{F}^{-T}$. The volumetric force in mechanical equilibrium with the exact first Piola–Kirchhoff stress tensor $\boldsymbol{P}^{\text{exact}}$ is

$$\boldsymbol{f}_0 = -\text{DIV} \boldsymbol{P}^{\text{exact}} \tag{A.5}$$

An explicit expression for $\boldsymbol{f}_0$ can be obtained using the chain rule as follows

$$\boldsymbol{f}_0 = -\text{DIV} \boldsymbol{P}^{\text{exact}} = -\left(\left.\frac{\partial \boldsymbol{P}^{\text{exact}}}{\partial \boldsymbol{F}}\right|_{\boldsymbol{F}^{\text{exact}}}\right)_{iIjJ} \frac{\partial\left(\boldsymbol{F}^{\text{exact}}\right)_{jJ}}{\partial X_I} \tag{A.6}$$

The non-zero term of the third order tensor $\frac{\partial \boldsymbol{F}}{\partial \boldsymbol{X}}$ are

$$\frac{\partial F_{11}}{\partial X_1} = 6AX_1; \quad \frac{\partial F_{22}}{\partial X_2} = 6BX_2; \quad \frac{\partial F_{33}}{\partial X_3} = 6CX_3; \quad \frac{\partial F_{21}}{\partial X_1} = 6X_1; \tag{A.7}$$

and the stiffness tensor $\frac{\partial \boldsymbol{P}^{\text{exact}}}{\partial \boldsymbol{F}}$ is obtained as follows

$$\begin{aligned}\left(\left.\frac{\partial \boldsymbol{P}^{\text{exact}}}{\partial \boldsymbol{F}}\right|_{\boldsymbol{F}^{\text{exact}}}\right)_{iIjJ} = {} & \mu \mathcal{I}_{iIjJ} + \frac{\mu}{\det \boldsymbol{F}^{\text{exact}2}} \left(\boldsymbol{H}^{\text{exact}}\right)_{iI} \left(\boldsymbol{H}^{\text{exact}}\right)_{jJ} \\ & - \mathcal{E}_{jpq} \mathcal{E}_{JPQ} \mathcal{I}_{iIpP} \left(\frac{\mu}{\det \boldsymbol{F}^{\text{exact}}} \boldsymbol{F}^{\text{exact}}\right)_{qQ}\end{aligned} \tag{A.8}$$

where $\mathcal{I}_{iIjJ} = \delta_{ij}\delta_{IJ}$ and $\boldsymbol{\mathcal{E}}$ represents the third order alternating tensor or Levi-Civita tensor. In addition, Dirichlet boundary conditions compatible with the displacement field must be provided,

$$\boldsymbol{u} = \boldsymbol{u}^{\text{exact}}; \qquad \text{on } \partial_D \Omega_0 \tag{A.9}$$

as well as a traction $\boldsymbol{t}_0$ on the Neumann portion of the boundary $\partial_N \Omega_0$,

$$\boldsymbol{t}_0 = \boldsymbol{P}^{\text{exact}} \boldsymbol{N}; \qquad \text{on } \partial_N \Omega_0 \tag{A.10}$$

where $\boldsymbol{N}$ is the unit normal vector to the boundary $\partial_N \Omega_0$.

The domain Ω is defined by $0 \leq X_1 \leq 10$, $0 \leq X_2 \leq 10$, $0 \leq X_3 \leq 0.43$ (in units of meters). The direction X_3 represents the thickness of the wedge elements. The boundary conditions in the Dirichlet and Neumann boundaries are:

$$\begin{aligned}\partial_D \Omega &= \left\{X_1 = 0 \cup X_2 = 0 \cup X_3 = 0\right\}; \\ \partial_N \Omega &= \left\{X_1 = 10 \cup X_2 = 10 \cup X_3 = 10\right\}\end{aligned} \tag{A.11}$$

Two structured grids in the $X_1 X_2$ plane are considered for the convergence study: a coarser grid of 5 × 5 elements and a finer grid of 10 × 10 elements.

Table B.1
Material parameters for validation with axisymmetric theory. These parameters correspond to the material parameters for a human descending aorta reported in Roccabianca et al. (2014).

c (kPa)	c_1^1 (kPa)	c_2^1	c_1^2 (kPa)	c_2^2	$c_1^{3,4}$ (kPa)	$c_2^{3,4}$	α_0 (deg)
37.20	4.68e−6	2.97e−7	2.9e−5	1.68e−5	28.16	3.48	43.88

Table B.2
Material parameters of the four-fiber constitutive model for wild type mice for different aortic wall segments denoted by ATA-Ascending Thoracic Aorta, DTA-Descending Thoracic Aorta, SAA-Suprarenal Abdominal Aorta, IAA-Infrarenal Abdominal Aorta, and CCA-Common Carotid Arteries (Roccabianca et al., 2014).

Wall segment	c (kPa)	c_1^1 (kPa)	c_2^1	c_1^2 (kPa)	c_2^2	$c_1^{3,4}$ (kPa)	$c_2^{3,4}$	α_0 (deg)	h (μm)
ATA	20.99	18.50	0.026	18.91	0.062	4.90	0.410	40.7	53.4
DTA	12.74	25.10	0.170	14.36	0.062	0.43	1.935	23.3	47.0
CCA	5.05	20.59	0.054	7.66	0.044	0.02	1.522	34.1	28.0

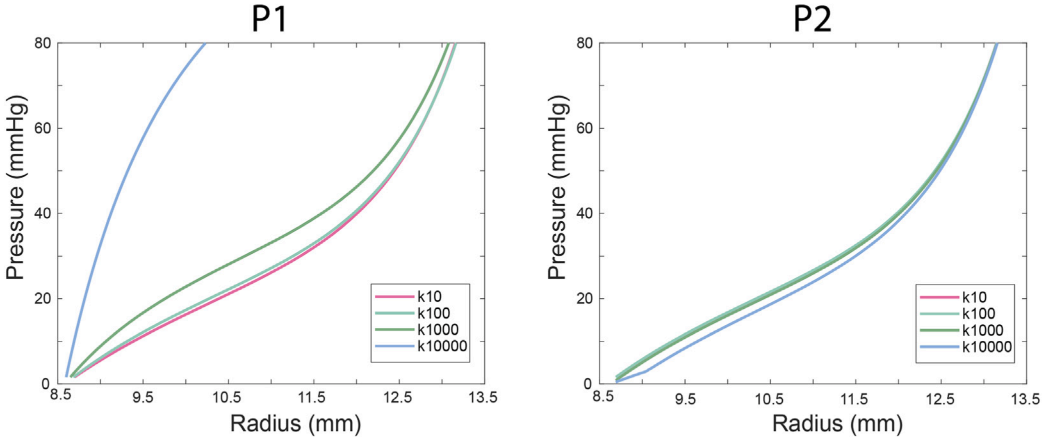

Fig. C.1. Sensitivity analysis of the penalty parameter k used to enforce incompressibility in the 3D formulations.

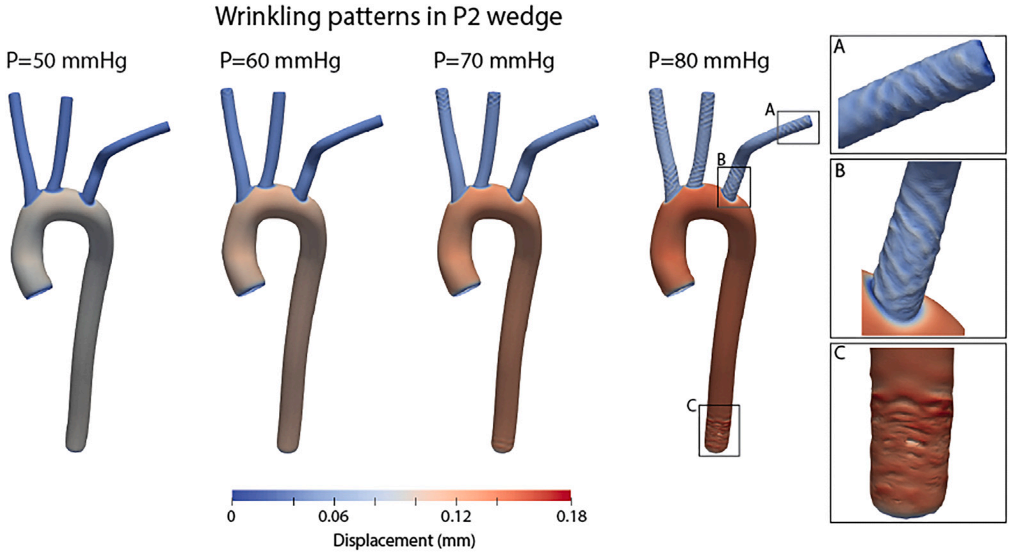

Fig. D.1. Wrinkling patterns in P2 wedge with insufficient external tissue support value.

Appendix B. Material parameters for the four-fiber family constitutive model

See Tables B.1 and B.2.

Appendix C. Sensitivity analysis for incompressibility term in the 3D formulations

In the P1 and P2 wedge 3D formulations, a penalty parameter k is introduced in the volumetric term to enforce the incompressibility condition. We calibrated this parameter using the cylindrical geometry problem described in Section 3.2 of the main manuscript. Different values of penalty parameters were tested: 10, 100, 1000, and 10,000 kPa. Fig. C.1 shows the pressure-radius results for the P1 and P2 wedge. For the P2 wedge, results shows consistent solutions across the different k values. However, the P1 wedge shows large discrepancies between low and high k values. These discrepancies, apparent for larger penalty terms, indicate the presence of volumetric locking. Based on these results, we used a value of $k = 100$ for the penalty parameter.

Appendix D. Wrinkling pattern in wedge formulation

In the mouse-specific geometry, the P2 wedge formulation exhibited wrinkling patterns at the side vessels and at the end of the main aorta under high pressure when small external tissue support values were used ($k_s = 0.6 \times 10^5$ g/(mm^2 s^2) and $k_s = 1.5 \times 10^5$ g/(mm^2 s^2) for the main aorta and side vessels, respectively). Fig. D.1 shows the P2 wedge results at four different pressure values: 50 mmHg (6.66 kPa), 60 mmHg (8.00 kPa), 70 mmHg (9.33 kPa), and 80 mmHg (10.66 kPa). Wrinkling patterns begin to appear around 60 mmHg and become increasingly severe and widespread at 80 mmHg. These patterns are only observed in the P2 wedge formulation and do not occur in the rotation-free shell or P1 wedge formulations. Increasing the external tissue support value helps to prevent wrinkling. The final external tissue support values are $k_s = 1.2{\times}10^5$ g/(mm^2 s^2) and $k_s = 3.0{\times}10^5$ g/(mm^2 s^2) for the main aorta and side vessels, respectively.

Data availability

Data will be made available on request.

References

Afazov, S., Becker, A., Hyde, T., 2012. Mathematical modeling and implementation of residual stress mapping from microscale to macroscale finite element models. J. Manuf. Sci. Eng. 134 (2).

Arthurs, C.J., Khlebnikov, R., Melville, A., Marčan, M., Gomez, A., Dillon-Murphy, D., Cuomo, F., Silva Vieira, M., Schollenberger, J., Lynch, S.R., Tossas-Betancourt, C., Iyer, K., Hopper, S., Livingston, E., Youssefi, P., Noorani, A., Ben Ahmed, S., Nauta, F.J.H., van Bakel, T.M.J., Ahmed, Y., van Bakel, P.A.J., Mynard, J., Di Achille, P., Gharahi, H., Lau, K.D., Filonova, V., Aguirre, M., Nama, N., Xiao, N., Baek, S., Garikipati, K., Sahni, O., Nordsletten, D., Figueroa, C.A., 2021. CRIMSON: An open-source software framework for cardiovascular integrated modelling and simulation. PLoS Comput. Biol. 17 (5), 1–21.

Bathe, M., Kamm, R., 1999. A fluid-structure interaction finite element analysis of pulsatile blood flow through a compliant stenotic artery. J. Biomech. Eng. 121 (4), 361–369.

Bazilevs, Y., Hsu, M.-C., Zhang, Y., Wang, W., Liang, X., Kvamsdal, T., Brekken, R., Isaksen, J., 2010. A fully-coupled fluid-structure interaction simulation of cerebral aneurysms. Comput. Mech. 46 (1), 3–16.

Behzadinasab, M., Alaydin, M., Trask, N., Bazilevs, Y., 2022. A general-purpose, inelastic, rotation-free Kirchhoff–Love shell formulation for peridynamics. Comput. Methods Appl. Mech. Engrg. 389, 114422.

Bellini, C., Ferruzzi, J., Roccabianca, S., Di Martino, E., Humphrey, J., 2014. A microstructurally motivated model of arterial wall mechanics with mechanobiological implications. Ann. Biomed. Eng. 42 (3), 488–502.

Bischoff, M., Bletzinger, K.-U., Wall, W., Ramm, E., 2004. Models and finite elements for thin-walled structures. Encycl. Comput. Mech..

Boffi, D., Brezzi, F., Fortin, M., et al., 2013. Mixed Finite Element Methods and Applications, vol. 44, Springer.

Bonet, J., Gil, A., Wood, R., 2016. Nonlinear Solid Mechanics for Finite Element Analysis: Statics. Cambridge University Press.

Cardamone, L., Valentin, A., Eberth, J., Humphrey, J., 2009. Origin of axial prestretch and residual stress in arteries. Biomech. Model. Mechanobiol. 8, 431–446.

Chen, K.-K., 2004. Comparison of shell and solid models for corner fill in tube hydroforming. In: AIP Conference Proceedings, vol. 712, (1), American Institute of Physics, pp. 1083–1088.

Colciago, C.M., Deparis, S., Quarteroni, A., 2014. Comparisons between reduced order models and full 3D models for fluid–structure interaction problems in haemodynamics. J. Comput. Appl. Math. 265, 120–138.

Cuomo, F., Ferruzzi, J., Agarwal, P., Li, C., Zhuang, Z.W., Humphrey, J.D., Figueroa, C.A., 2019. Sex-dependent differences in central artery haemodynamics in normal and fibulin-5 deficient mice: implications for ageing. Proc. R. Soc. A 475 (2221), 20180076.

de Lucio, M., García, M.F., García, J.D., Rodríguez, L.E.R., Marcos, F.Á., 2021. On the importance of tunica intima in the aging aorta: a three-layered in silico model for computing wall stresses in abdominal aortic aneurysms. Comput. Methods Biomech. Biomed. Eng. 24 (5), 467–484.

Demiray, H., Vito, R.P., 1991. A layered cylindrical shell model for an aorta. Internat. J. Engrg. Sci. 29 (1), 47–54.

Diaz, C., Pena, J.A., Martinez, M.A., Pena, E., 2021. Unraveling the multilayer mechanical response of aorta using layer-specific residual stresses and experimental properties. J. Mech. Behav. Biomed. Mater. 113, 104070.

Dobrin, P., Canfield, T., Sinha, S., 1975. Development of longitudina retraction of carotid arteries in neonatal dogs. Experientia 31 (11), 1295–1296.

Doyle, B.J., Callanan, A., McGloughlin, T.M., 2007. A comparison of modelling techniques for computing wall stress in abdominal aortic aneurysms. Biomed. Eng. Online 6 (1), 1–12.

Eberth, J., Cardamone, L., Humphrey, J., 2011. Evolving biaxial mechanical properties of mouse carotid arteries in hypertension. J. Biomech. 44 (14), 2532–2537.

Ferruzzi, J., Collins, M.J., Yeh, A.T., Humphrey, J.D., 2011. Mechanical assessment of elastin integrity in fibrillin-1-deficient carotid arteries: implications for marfan syndrome. Cardiovasc. Res. 92 (2), 287–295.

Figueroa, C.A., Baek, S., Taylor, C.A., Humphrey, J.D., 2009. A computational framework for fluid–solid-growth modeling in cardiovascular simulations. Comput. Methods Appl. Mech. Engrg. 198 (45–46), 3583–3602.

Figueroa, C.A., Vignon-Clementel, I.E., Jansen, K.E., Hughes, T.J., Taylor, C.A., 2006. A coupled momentum method for modeling blood flow in three-dimensional deformable arteries. Comput. Methods Appl. Mech. Engrg. 195 (41–43), 5685–5706.

Flores, F.G., Onate, E., 2005. Improvements in the membrane behaviour of the three node rotation-free BST shell triangle using an assumed strain approach. Comput. Methods Appl. Mech. Engrg. 194 (6–8), 907–932.

Gerbeau, J.-F., Vidrascu, M., Frey, P., 2005. Fluid–structure interaction in blood flows on geometries based on medical imaging. Comput. Struct. 83 (2–3), 155–165.

Gil, A.J., 2006. Structural analysis of prestressed saint venant–Kirchhoff hyperelastic membranes subjected to moderate strains. Comput. Struct. 84 (15–16), 1012–1028.

Gil, A.J., Bonet, J., 2006. Finite element analysis of prestressed structural membranes. Finite Elem. Anal. Des. 42 (8–9), 683–697.

Gil, A.J., Bonet, J., 2007. Finite element analysis of partly wrinkled reinforced prestressed membranes. Comput. Mech. 40, 595–615.

Giudici, A., Spronck, B., 2022. The role of layer-specific residual stresses in arterial mechanics: analysis via a novel modelling framework. Artery Res. 28 (2), 41–54.

Gruttmann, F., Taylor, R., 1992. Theory and finite element formulation of rubberlike membrane shells using principal stretches. Internat. J. Numer. Methods Engrg. 35 (5), 1111–1126.

Holzapfel, G.A., Gasser, T.C., Ogden, R.W., 2000. A new constitutive framework for arterial wall mechanics and a comparative study of material models. J. Elast. Phys. Sci. Solids 61 (1–3), 1–48.

Holzapfel, G.A., Gasser, T.C., Ogden, R.W., 2004. Comparison of a multi-layer structural model for arterial walls with a fung-type model, and issues of material stability. J. Biomech. Eng. 126 (2), 264–275.

Holzapfel, G.A., Ogden, R.W., 2010. Modelling the layer-specific three-dimensional residual stresses in arteries, with an application to the human aorta. J. R. Soc. Interface 7 (46), 787–799.

Hosseini, S., Remmers, J.J., Verhoosel, C.V., De Borst, R., 2013. An isogeometric solid-like shell element for nonlinear analysis. Internat. J. Numer. Methods Engrg. 95 (3), 238–256.

Hosseini, S., Remmers, J.J., Verhoosel, C.V., De Borst, R., 2014. An isogeometric continuum shell element for non-linear analysis. Comput. Methods Appl. Mech. Engrg. 271, 1–22.

Hron, J., Mádlík, M., 2007. Fluid-structure interaction with applications in biomechanics. Nonlinear Anal. Real World Appl. 8 (5), 1431–1458.

Hughes, T.J., Carnoy, E., 1983. Nonlinear finite element shell formulation accounting for large membrane strains. Comput. Methods Appl. Mech. Engrg. 39 (1), 69–82.

Humphrey, J.D., 2013. Cardiovascular Solid Mechanics: Cells, Tissues, and Organs. Springer Science & Business Media.

Humphrey, J., Rajagopal, K., 2002. A constrained mixture model for growth and remodeling of soft tissues. Math. Models Methods Appl. Sci. 12 (03), 407–430.

Kiendl, J., Bletzinger, K.-U., Linhard, J., Wüchner, R., 2009. Isogeometric shell analysis with Kirchhoff–Love elements. Comput. Methods Appl. Mech. Engrg. 198 (49–52), 3902–3914.

Kiendl, J., Hsu, M.-C., Wu, M.C., Reali, A., 2015. Isogeometric Kirchhoff–Love shell formulations for general hyperelastic materials. Comput. Methods Appl. Mech. Engrg. 291, 280–303.

Kim, H., Lu, J., Sacks, M.S., Chandran, K.B., 2008. Dynamic simulation of bioprosthetic heart valves using a stress resultant shell model. Ann. Biomed. Eng. 36 (2), 262–275.

Kim, T., Tjahjadi, N.S., He, X., van Herwaarden, J., Patel, H.J., Burris, N.S., Figueroa, C.A., 2023b. Three-dimensional characterization of aortic root motion by vascular deformation mapping. J. Clin. Med. 12 (13), 4471.

Kim, T., van Bakel, P.A.J., Nama, N., Burris, N., Patel, H.J., Williams, D.M., Figueroa, C.A., 2023a. A computational study of dynamic obstruction in type b aortic dissection. J. Biomech. Eng. 145 (3), 031008.

Kyriacou, S., Humphrey, J., Schwab, C., 1996. Finite element analysis of nonlinear orthotropic hyperelastic membranes. Comput. Mech. 18 (4), 269–278.

Lally, C., Dolan, F., Prendergast, P., 2005. Cardiovascular stent design and vessel stresses: a finite element analysis. J. Biomech. 38 (8), 1574–1581.

Laubrie, J.D., Mousavi, J.S., Avril, S., 2020. A new finite-element shell model for arterial growth and remodeling after stent implantation. Int. J. Numer. Methods Biomed. Eng. 36 (1), e3282.

Liu, M., Liang, L., Sun, W., 2017. A new inverse method for estimation of in vivo mechanical properties of the aortic wall. J. Mech. Behav. Biomed. Mater. 72, 148–158.

Lu, K., Accorsi, M., Leonard, J., 2001. Finite element analysis of membrane wrinkling. Internat. J. Numer. Methods Engrg. 50 (5), 1017–1038.

Lu, J., Zhou, X., Raghavan, M.L., 2007. Inverse elastostatic stress analysis in pre-deformed biological structures: demonstration using abdominal aortic aneurysms. J. Biomech. 40 (3), 693–696.

Lu, J., Zhou, X., Raghavan, M.L., 2008. Inverse method of stress analysis for cerebral aneurysms. Biomech. Model. Mechanobiol. 7 (6), 477–486.

Maas, S.A., Ellis, B.J., Ateshian, G.A., Weiss, J.A., 2012. FEBio: finite elements for biomechanics. J. Biomech. Eng. 134 (1).

Martin, C., Sun, W., Elefteriades, J., 2015. Patient-specific finite element analysis of ascending aorta aneurysms. Am. J. Physiology-Heart Circ. Physiol. 308 (10), H1306–H1316.

Meftah, K., Sedira, L., Ayadi, A., 2021. A six-node prismatic solid finite element for geometric nonlinear problems in elasticity. Math. Comput. Simulation 182, 143–164.

Nama, N., Aguirre, M., Humphrey, J.D., Figueroa, C.A., 2020. A nonlinear rotation-free shell formulation with prestressing for vascular biomechanics. Sci. Rep. 10 (1), 17528.

Oñate, E., Flores, F.G., 2005. Advances in the formulation of the rotation-free basic shell triangle. Comput. Methods Appl. Mech. Engrg. 194 (21–24), 2406–2443.

Ortigosa, R., Gil, A.J., Lee, C.H., 2016. A computational framework for large strain nearly and truly incompressible electromechanics based on convex multi-variable strain energies. Comput. Methods Appl. Mech. Engrg. 310, 297–334.

Poya, R., Ortigosa, R., Gil, A.J., 2023. Variational schemes and mixed finite elements for large strain isotropic elasticity in principal stretches: Closed-form tangent eigensystems, convexity conditions, and stabilised elasticity. Internat. J. Numer. Methods Engrg. 124 (16), 3436–3493.

Poya, R., Sevilla, R., Gil, A.J., 2016. A unified approach for a posteriori high-order curved mesh generation using solid mechanics. Comput. Mech. 58, 457–490.

Raghavan, M.L., Vorp, D.A., Federle, M.P., Makaroun, M.S., Webster, M.W., 2000. Wall stress distribution on three-dimensionally reconstructed models of human abdominal aortic aneurysm. J. Vasc. Surg. 31 (4), 760–769.

Remmers, J.J., Wells, G.N., Borst, R.d., 2003. A solid-like shell element allowing for arbitrary delaminations. Internat. J. Numer. Methods Engrg. 58 (13), 2013–2040.

Riveros, F., Chandra, S., Finol, E.A., Gasser, T.C., Rodriguez, J.F., 2013. A pull-back algorithm to determine the unloaded vascular geometry in anisotropic hyperelastic AAA passive mechanics. Ann. Biomed. Eng. 41 (4), 694–708.

Roccabianca, S., Figueroa, C., Tellides, G., Humphrey, J., 2014. Quantification of regional differences in aortic stiffness in the aging human. J. Mech. Behav. Biomed. Mater. 29, 618–634.

Schroeder, F., Polzer, S., Slažanskỳ, M., Man, V., Skácel, P., 2018. Predictive capabilities of various constitutive models for arterial tissue. J. Mech. Behav. Biomed. Mater. 78, 369–380.

Tepole, A.B., Kabaria, H., Bletzinger, K.-U., Kuhl, E., 2015. Isogeometric Kirchhoff–Love shell formulations for biological membranes. Comput. Methods Appl. Mech. Engrg. 293, 328–347.

Von Maltzahn, W.-W., Besdo, D., Wiemer, W., 1981. Elastic properties of arteries: a nonlinear two-layer cylindrical model. J. Biomech. 14 (6), 389–397.

Weisbecker, H., Pierce, D.M., Holzapfel, G.A., 2014. A generalized prestressing algorithm for finite element simulations of preloaded geometries with application to the aorta. Int. J. Numer. Methods Biomed. Eng. 30 (9), 857–872.

Wriggers, P., Eberlein, R., Reese, S., 1996. A comparison of three-dimensional continuum and shell elements for finite plasticity. Int. J. Solids Struct. 33 (20–22), 3309–3326.

Yamakawa, S., Shimada, K., 2009. Converting a tetrahedral mesh to a prism–tetrahedral hybrid mesh for FEM accuracy and efficiency. Internat. J. Numer. Methods Engrg. 80 (1), 74–102.

Zhou, X., Raghavan, M.L., Harbaugh, R.E., Lu, J., 2010. Patient-specific wall stress analysis in cerebral aneurysms using inverse shell model. Ann. Biomed. Eng. 38 (2), 478–489.

Zienkiewicz, O.C., Taylor, R.L., Zhu, J.Z., 2005. The Finite Element Method: Its Basis and Fundamentals. Elsevier.